Elsevier Editorial System(tm) for Journal of Alloys and Compounds

Manuscript Draft

Manuscript Number: JALCOM-D-16-04442R1

Title: Photoluminescent Properties of ZrO2: Tm3+, Tb3+, Eu3+ Powders—A Combined Experimental and Theoretical Study.

Article Type: Full Length Article

Keywords: ZrO2: RE; photoluminescence; DFT Calculations; white LEDs.

Corresponding Author: Dr. laura lovisa, Ph.D.

Corresponding Author's Institution: universidade federal do rio grande do norte

First Author: laura lovisa, Ph.D.

Order of Authors: laura lovisa, Ph.D.; Juan Andrés, Ph.D.; Lourdes Gracia, Ph.D.; Maximo Li, Ph.D.; Carlos Paskocimas, Ph.D.; Maurício Bomio, Ph.D.; Vinicius Araujo, Ph.D.; Elson Longo, Ph.D.; Fabiana Motta, Ph.D.

Abstract: Rare-earth (RE) element-based materials for optical applications have received increasing attention owing to the emission properties of RE ions, which render these materials suitable for use in color displays, lasers, and solid-state lighting. In the present work, ZrO2:RE (RE =Tm3+, Tb3+, and Eu3+) powders were obtained via complex polymerization, and characterized by means of X-ray diffraction (XRD), Raman spectroscopy, UV-visible absorption spectroscopy, and photoluminescence measurements. The XRD patterns and Raman spectra revealed the tetragonal phase of ZrO2 co-doped with up to 4 mol.% RE3+ and stabilization of the cubic phase, for up to 8 mol.% RE3+. In addition, the photoluminescence measurements revealed simultaneous emissions in the blue (477 nm), green (496.02 nm and 548.32 nm), and red-orange (597.16 nm and 617.54 nm) regions. These emissions result from the Tm3+, Tb 3+, and Eu3+ ions, respectively. Energy transfers, such as 1G4 levels (Tm3+) → 5D4 (Tb3+) and 5D4 levels (Tb3+) → 5D0 (Eu3+), occurred during the emission process. Calculations based on density functional theory (DFT) were performed, to complement the experimental data. The results revealed that structural order/disorder effects were generated in the cubic and tetragonal ZrO2 phases in the ZrO2:Eu3+ powders, and changes in the electronic structure were manifested as a decrease in the band gap values. The chromaticity coordinates of all the samples were determined from the PL spectrum. The coordinates, x = 0.34 and y = 0.34, of the ZrO2:8%RE sample corresponded to a point located in the white region of the CIE diagram and color correlated temperature (CCT) was found to be 5181K. More importantly, the present results indicate that ZrO2:RE powders constitute promising photoluminescent materials for use in new lighting devices.

UNIVERSIDADE FEDERAL DO RIO GRANDE DO NORTE
CENTRO DE TECNOLOGIA

DEPARTAMENTO DE ENGENHARIA DE MATERIAIS

To Editor:

Dr. L. Schultz

Scientific Director, IFW Dresden, Germany

Natal, May, 11, 2016

Dear Prof. Dr. L. Schultz,

Please, find enclosed the original manuscript entitled "**Photoluminescent Properties of ZrO_2: Tm^{3+}, Tb^{3+}, Eu^{3+} Powders—A Combined Experimental and Theoretical Study"** by the authors L. X. Lovisa, J. Andrés, L. Gracia, M. S. Li, C. A. Paskocimas, M. R. D. Bomio, V. D. Araujo, E. Longo and F. V. Motta. In our manuscript, we describe the preparation of ZrO_2 co-doped with Tm^{3+}/Tb^{3+}/Eu^{3+} powders by the Complex Polymerization Method (CPM). We analyzed the effect of concentration of dopants on the optical properties. According to the CIE diagram, the CIE coordenates calculated to samples are located in the white region. The results demonstrate the presence of order/disorder effects generated in the cubic and tetragonal ZrO_2 phases in ZrO2:Eu^{3+}, while changes in the electronic structure were also sensed with a decrease in the band gap values. The ZrO_2:RE materials are promising photoluminescent materials for applications in new lighting devices. The powders were characterized by X-ray diffraction, reflectance spectroscopy in uv-visible and photoluminescent (PL). We would like to submit this manuscript for publication in the ***Journal of Alloys and Compounds.***

We wish you a good reception and we look forward to hearing from you.

Yours sincerely,

Dr. Lovisa, L. X.
Department of Materials – DEMAT/UFRN
Av. Sen. Salgado Filho, 3000 - Campus Universitário
59072-970 - Natal/RN
Tel/fax: +55-84-3342-2406
e-mail: lovisaengmat@ig.com.br

UNIVERSIDADE FEDERAL DO RIO GRANDE DO NORTE
CENTRO DE TECNOLOGIA

DEPARTAMENTO DE ENGENHARIA DE MATERIAIS

To Editor:

Dr. L. Schultz
Scientific Director, IFW Dresden, Germany

Natal, November, 14, 2016

Dear Prof. Dr. L. Schultz**,**

We performed request revisions and we are sending the revised manuscript (JALCOM-D-16-04442) "**Photoluminescent Properties of ZrO_2: Tm^{3+}, Tb^{3+}, Eu^{3+} Powders—A Combined Experimental and Theoretical Study"** by the authors L. X. Lovisa, J. Andrés, L. Gracia, M. S. Li, C. A. Paskocimas, M. R. D. Bomio, V. D. Araujo, E. Longo and F. V. Motta.

With Best Regards,

JALCOM-D-16-04442

Yours sincerely,

Dr. Lovisa, L. X.
Department of Materials – DEMAT/UFRN
Av. Sen. Salgado Filho, 3000 - Campus Universitário
59072-970 - Natal/RN
Tel/fax: +55-84-3342-2406
e-mail: lovisaengmat@ig.com.br

Natal, 30, October 2016.

Title: Photoluminescent Properties of ZrO_2: Tm^{3+}, Tb^{3+}, Eu^{3+} Powders—A Combined Experimental and Theoretical Study

Authors: L. X. Lovisa, J. Andrés, L. Gracia, M. S. Li, C. A. Paskocimas, M. R. D. Bomio, V. D. Araujo, E. Longo and F. V. Motta

Response to Reviews:

Firstly, we would like to thank to reviewers for the collaboration in the improvement of the work. The modifications were accomplished to enrich this study (JALCOM-D-16-04442). The manuscript was totally revised and specifics corrections were based on the reviewer suggestions.

The response to the comments of Reviewers and the corrections are listed below.

Reviewer #1:

(1) In the abstract, page 4 / line 2, the authors claim that there is energy transfer from $^1G_4$ levels (Tm^{3+}) to $^5D_4$ (Tb^{3+}), but this is not discussed on page 16 (section 3.5). This is also not represented in Figure 8.

Answer:

"The energy level $^5D_4$ of Tb^{3+} is very close to the energy level of Tm^{3+} $^1G_4$ as seen in the energy diagram (Figure 8). This setting energy levels contributes to efficient energy transfer process (ET1) between Tm^{3+} ions and Tb^{3+} [78]. The $^1G_4$ level of Tm^{3+} is completely filled by the charge carriers (electrons) from the excitation process (λ = 350 nm). The increased concentration of Tm^{3+} promotes the increase of the intensity of the transition $^1G_4 \rightarrow {}^3H_6$, this increased intensity of Tm^{3+} also acts as a source for transporting

energy for the sublevel $^5D_4$ of Tb^{3+}, this effect is realized by increasing the intensity of transition $^5D_4 \rightarrow {}^7F_5$ (550 nm) Tb^{3+}, shown in Figure 7."

Figure 8 has been corrected as the reviewer's suggestion

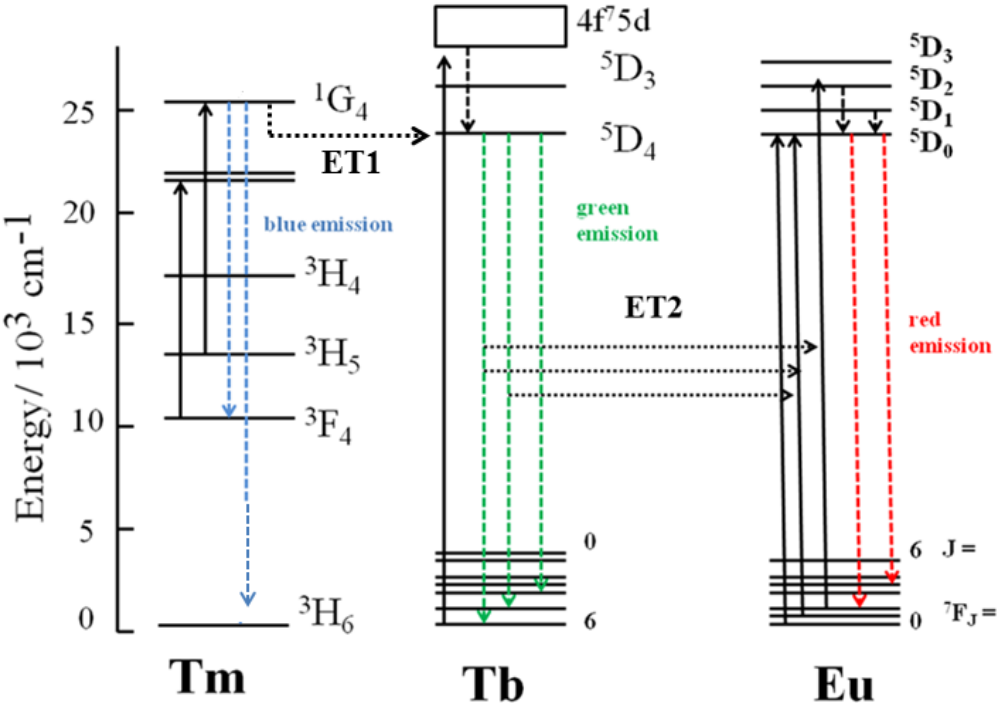

(2) Page 7, line 7: it looks like is missing a reference "(CITA)"

Answer:

It was added the following reference:

15. S. Mukherjee, D. P. Dutta, N. Manoj, A. K. Tyagi, Sonochemically synthesized rare earth double-doped zirconia nanoparticles: probable candidate for white light emission, J Nanopart Res 14 (2012) 814.

(3) In page 11, section 3.1, the authors refer to three samples with xRE of 1,2 and 4%, but depict four diffractograms (Fig.1 a b c and d). It looks like Figure 1d refers to a sample with xRE of 6%, that is not discussed in this paper. So the authors must revise these data and the figure 1.

Answer:

The four diffractograms shown in Figure 1 (a) - (d) correspond respectively to the samples undoped ZrO_2, ZrO_2: 1%RE, ZrO_2: 2%RE and ZrO_2: 4%RE, the tetragonal phase of ZrO_2. Figure 1 (e) is the sample ZrO_2: 8%RE, the cubic phase of ZrO_2. At no time was quoted sample doped to 6%RE. These results have been properly discussed in section 3.1.

(4) 81-1551 and 81-1446 are not ICSD collection code numbers, but JCPDS. The correct ICSD numbers are: (ICSD_72956 for JCPDS_811581) and (ICSD_72951 for JCPDS_811546). The authors can choose which code to use, but with the correct numbers.

(5) Despite the relatively low quality of the XRD patterns, in Figure 1(a) is possible to identify a low-intensity peak at about 43 degrees, which is characteristic of tetragonal ZrO2 phase.

Answer (4) and (5):

Changes in XRD reference card were made as suggested. ICSD_72956 to Figure 1 (a-d) indicating the tetragonal phase and ICSD_72951 to Figure 1 (e) indicating the cubic phase as well as the identified peak (102) located 44.22º to tetragonal phase of ZrO_2.

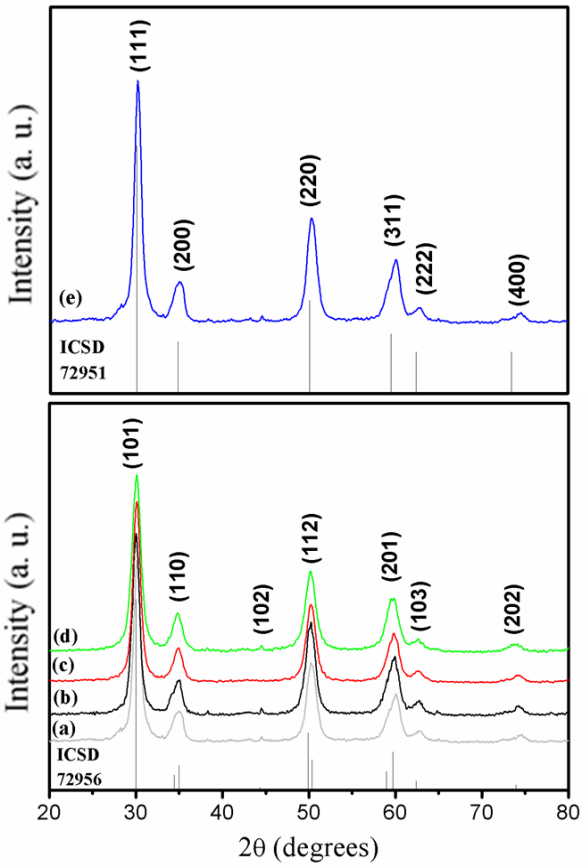

(6) In Figure 1 are presented five diffractograms, but in Figure 2 only four Raman spectra, the authors must be sure that these spectra were correctly named.

Answer:

The Raman spectroscopic analysis was used to confirm the results obtained by XRD, Raman since it is a very sensitive technique to detect structural changes of the materials. On this purpose, analyzes were performed for samples co-doped 1, 2, 4 and 8% of rare earths (RE) in order to verify phase transition from tetragonal → cubic. The result met the expected. The sample with higher dopant content (8% RE) is stabilized in the cubic phase. This result is consistent with other studies in the literature:

(I) C. G. Kontoyannis, Quantitative determination of the cubic, tetragonal and monoclinic phases in partially stabilized zirconias by Raman spectroscopy, Journal of materials science 29 (1994) 5316-5320.

(II) D. Bersani et al., Micro-Raman study of indium doped zirconia obtained by sol–gel, Journal of Non-Crystalline Solids, 345–346(2004) 116-119.

(III) C. Wulfman, M. Sadoun and M. Lamy de la Chapelle, Interest of Raman spectroscopy for the study of dental material: The zirconia material example, IRBM, 31(2010) 257-262.

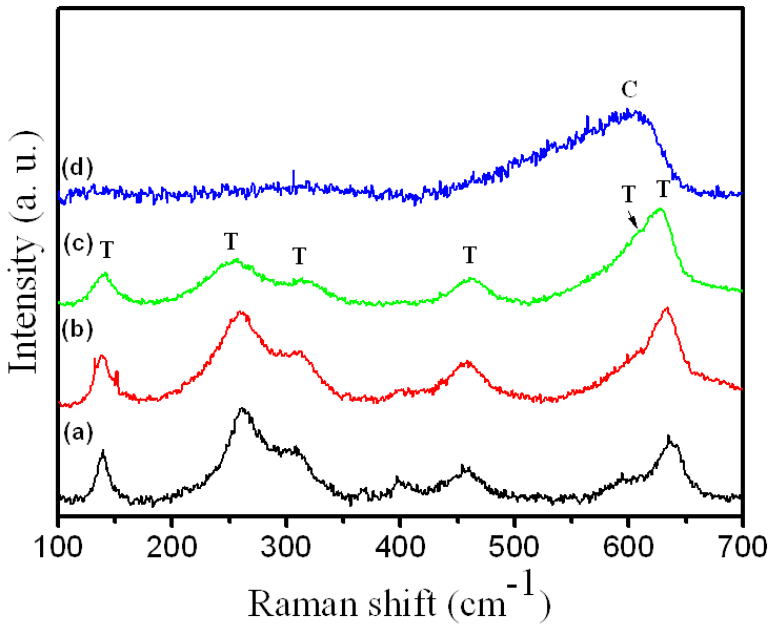

(7) In page 18, line 7-9, the authors attributed the white luminescence of the ZrO_2 matrix to the RE ions Tm^{3+}, Tb^{3+} and Eu^{3+}, but, in my opinion, the self-activated luminescence from ZrO_2 matrix is very important and it must be highlighted.

Answer:

"It is observed in Figure 7 for the sample ZrO_2: 8% RE the photoluminescent behavior of ZrO_2 host was very significant. The presence of oxygen vacancies (V_0) in the matrix is responsible for the emergence of broadband emission at around 450 nm [87]. The oxygen vacancy always leads to formation of energy levels within the band gap. When ZrO_2 is excited by a photon, the electrons are trapped by V_0 and centers are created (F) [88]. Then recombination centers (F) with the holes (h^+) creates the transmitter excited states. From these states originate transitions which decay to a state with lower energy level. The band of blue emission from the ZrO_2 contributes along with the specific emission of rare earth on white emission as shown in Figure 8."

Reviewer 3:

The manuscript by Lovisa et al. reports on photoluminescent properties of ZrO_2 doped with T $^{3+}$, Tb^{3+}, and Eu^{3+}. To successfully tackle the problem, the authors characterized the powder samples by XRD, Raman spectroscopy, UV-visible absorption and PL spectroscopes. Additionally, the DFT calculations were performed to characterize stability of cubic and tetragonal structures of Eu-doped ZrO_2 as well as its electronic properties. Results of this work indicate that RE ions (Tm^{3+}, Tb^{3+}, and Eu^{3+}) can make ZrO_2 a potential material for light-emitting diodes.

I recommend publication of this paper after considering the following suggestions.

- For sake of completeness it would be beneficial to perform electronic structure calculations for Tm- and Tb-doped ZrO_2 and supplement the computational details section with valence configurations of Zr, O, and RE atoms used in computations.

Answer: Electronic structure calculations for Tm- and Tb-doped ZrO2 have been performed in the revised version of the manuscript (figures S1 has been added in the supplementary information). In addition, valence configurations of Zr, O, and RE atoms used in computations have been introduced in computational details.

- Results of the electronic structure calculations with the PL spectra could be compared in more detail.

Answer: Results of the electronic structure calculations with the PL spectra have been compared in more detail in the revised version of the manuscript.

- Some comments on the results of similar studies reported in Journal of Radiation Research and Applied Sciences 8, 11 (2015) could be added.

Answer: This reference has been cited and commented in the revised version of the manuscripts.

Photoluminescent Properties of ZrO_2: Tm^{3+}, Tb^{3+}, Eu^{3+} Powders—A Combined Experimental and Theoretical Study

L. X. Lovisa, *[a], J. Andrés [b], L. Gracia[b], M. S. Li[c], C. A. Paskocimas[a], M. R. D. Bomio[a], V. D. Araujo[d], E. Longo[e] and F. V. Motta[a]

[a]*DEMAT, CT, UFRN, Av. Sen. Salgado Filho, 3000, CEP 59072-970 Natal, RN, Brazil*

[b]*Departament de Química Física i Analítica, Universitat Jaume I, Campus del Riu Sec, Castelló E-12071, Spain*

[c]*IFSC, USP, Av. Trabalhador São Carlense, 400, CEP 13566-590 São Carlos, SP, Brazil*

[d]*UFRPE, Av. Rua Dom Manoel de Medeiros,CEP52171-900 Recife, PE – Brazil*

[e]*LIEC, IQ, UNESP, Rua Francisco Degni s/n, CEP 14801-907 Araraquara, SP, Brazil*

Abstract

Rare-earth (RE) element-based materials for optical applications have received increasing attention owing to the emission properties of RE ions, which render these materials suitable for use in color displays, lasers, and solid-state lighting. In the present work, ZrO_2:RE (RE =Tm^{3+}, Tb^{3+}, and Eu^{3+}) powders were obtained via complex polymerization, and characterized by means of X-ray diffraction (XRD), Raman spectroscopy, UV-visible absorption spectroscopy, and photoluminescence measurements. The XRD patterns and Raman spectra revealed the tetragonal phase of ZrO_2 co-doped with up to 4 mol.% RE^{3+} and stabilization of the cubic phase, for up to 8 mol.% RE^{3+}. In addition, the photoluminescence measurements revealed simultaneous emissions in the blue (477 nm), green (496.02 nm and 548.32 nm), and red-orange (597.16 nm and 617.54 nm) regions. These emissions result from the Tm^{3+}, Tb^{3+}, and Eu^{3+} ions, respectively. Energy transfers, such as $^1G_4$ levels (Tm^{3+}) → $^5D_4$ (Tb^{3+}) and $^5D_4$ levels (Tb^{3+}) → $^5D_0$ (Eu^{3+}), occurred during the emission process. Calculations

based on density functional theory (DFT) were performed, to complement the experimental data. The results revealed that structural order/disorder effects were generated in the cubic and tetragonal ZrO_2 phases in the ZrO_2:Eu^{3+} powders, and changes in the electronic structure were manifested as a decrease in the band gap values. The chromaticity coordinates of all the samples were determined from the PL spectrum. The coordinates, x = 0.34 and y = 0.34, of the ZrO_2:8%RE sample corresponded to a point located in the white region of the CIE diagram and color correlated temperature (CCT) was found to be 5181K. More importantly, the present results indicate that ZrO_2:RE powders constitute promising photoluminescent materials for use in new lighting devices.

Keywords: ZrO_2: RE; photoluminescence; DFT Calculations; white LEDs.

*Corresponding author. lovisaengmat@ig.com.br (L. X. Lovisa)

1. Introduction

The synthesis and characterization of rare earth (RE)-doped nanomaterials have been extensively investigated. These materials have excellent properties [1, 2], such as narrow emission bandwidths (<10 nm), long luminescence lifetime, high photostability, and low toxicity [3, 4]. In recent years, these materials have received considerable attention owing to their use in several important applications, such as multiplexed imaging and sensing, bioassays, and multiplex biodetection [5–14]. The development of luminescent materials, which are more efficient than those currently available, is extremely challenging. Moreover, the use of a suitable host material for the RE ions is essential for achieving high efficiency [15].

Zirconium dioxide or zirconia (ZrO_2) and ZrO_2-based materials constitute an appropriate host for RE, owing to a unique combination of different properties. These include: high refractive index, large optical band gap, low optical loss, and high transparency in the visible and near-infrared regions, good chemical stability [16–17], and lower phonon frequency (~470 cm^{-1}) than other matrices such as Y_2O_3 (~597 cm^{-1}) and TiO_2 (~700 cm^{-1}) [18]. As such, the luminescence efficiency of active ions may be improved via incorporation into the ZrO_2 matrix [19].

RE ions can enhance the emission of photoluminescent materials, and the corresponding energy transfer (ET) process occurs between an ion donor (D) and an ion acceptor (A). During the ET process, the energy of D (which is in an excited electronic state) is transferred to A. Specific conditions must be fulfilled in order to realize this mechanism. These include: (i) the emission band of D is partially superimposed on the absorption band of A, and (ii) the distance (R) between D and A must be sufficiently short, since the energy transfer efficiency is proportional to $1/R^6$, to enable interaction of the dipole–dipole emission bands of the material [20]. These unique properties have led to the widespread use of RE ions in optical devices.

Direct excitation of Eu^{3+} ions is a relatively inefficient process, owing to the forbidden nature of the 4f transitions. However, Eu-doped inorganic materials may exhibit efficient luminescence emissions upon ultraviolet excitation. These materials also exhibit a large Stokes shift, sharp emission spectrum, and have a long lifetime, high chemical/photochemical stability, low toxicity, and reduced photobleaching, owing to shielding of the 4f electrons [21]. As such, Quan et al. [22] obtained spherical ZrO_2:Eu^{3+} particles by using a spray drying process followed by a post annealing treatment. Gedanken et al. [23] used a sonochemical method for the europium-oxide doping of

ZrO_2 nanoparticles. Furthermore, Tiwari et al. [24] determined the effect of varying Eu^{3+} concentration on the photo- and thermoluminescence of ZrO_2 nanophosphors. Some RE ion-doped ZrO_2 materials, such as ZrO_2:Eu [25], ZrO_2:Tb [26], and ZrO_2:Tm [27], have interesting properties. Vidya et al. [28] investigated the color-tunable photoluminescence photocatalytic activities and phase transformation of a ZrO_2:Tb^{3+} nanophosphor. Mari et al. [29] determined the photoluminescence properties of Tb^{3+} in ZrO_2 zirconia host matrices (prepared via combustion synthesis) at different calcination temperatures.

Shang et al. [30] examined the process of energy transfer between Tm^{3+} and Ho^{3+} excited by a UV nanocrystal-LaOF laser and classified the interaction between the ions as a quadrupole-quadrupole type of interaction. Joshi [31] examined the energy transfer from Tb^{3+} and Eu^{3+} in zinc phosphate glasses and concluded that these ions undergo mainly dipole-dipole interactions. Moreover, the efficiency of this transfer was highest at a concentration of 8.6 mol% Eu^{3+}. The emissions of Tm^{3+}, Eu^{3+}, and Tb^{3+} ions fall within the blue, red, and green regions, respectively, of the visible spectrum [32–34]. Particles that have tunable emission colors are obtained from a combination of lanthanide ions in a host material. The first-ever generation of white light from the simultaneous emission of blue, green, and red, under UV excitation, was obtained for borate-based glasses co-doped with Ce^{3+}, Tb^{3+}, and Mn^{3+} [35]. Furthermore, the spectra of Tm^{3+}, Tb^{3+}, and Sm^{3+} co-doped silicate glass, which was excited in the near-UV region, exhibited bands corresponding to blue, green, and orange-red emissions [36].

This paper can be considered a prolongation of previously work (CITA) in which the main focus is the investigation of the photoluminescent properties of the particles of ZrO_2 co-doped with Tm^{3+}, Tb^{3+}, and Eu^{3+}, by using the polymerization method [37–40]. The use of the complex polymerization method in the research materials is widespread because it presents advantages such as good homogeneous distribution of different metal ions along the polymer formed, facilitating control stoichiometric. Other positive aspects of the method are the low temperature synthesis, obtaining nanometric particles and reproducibility.At this time, we will examine the effect of the concentration of RE (mol%) in the discussed property. In addition, first-principle calculations were performed in order to explain the structural and electronic changes induced by the doping of ZrO_2:Eu. The energy transfer processes between Tm^{3+} and Tb^{3+} and between Tb^{3+} and Eu^{3+}, were also discussed. X-ray diffraction (XRD), Raman spectroscopy, UV-visible reflectance spectroscopy, and photoluminescence (PL) measurements were used

to characterize the samples. Moreover, a chromaticity diagram was determined from emission spectra data, in order to verify the efficiency of these materials during the emission of white light.

The remainder of this paper is organized as follows: section 2 describes the synthesis method, characterization techniques, and computational details; sections 3 and 4 present the results and conclusions, respectively.

2. Experimental section

2.1 Synthesis of ZrO_2:RE powders

The samples were prepared by using a complex polymerization method. During the synthesis, the zirconium citrate was obtained by dissolving zirconium nitrate (Vetec, 99%) in an aqueous citric acid solution, under agitation, at a temperature of ~80 °C. Doping was performed by adding cations of RE to the solution. A europium solution and a thulium solution were prepared by dissolving Eu_2O_3 (Aldrich, 99.9%) and Tm_2O_3 (Aldrich, 99.9%), respectively, in nitric acid. Each solution was then separately mixed with the zirconium citrate solution. Terbium nitrate (Aldrich, 99.9%) was subsequently added to the mixed solution. Furthermore, ethylene glycol was added to the solution, under constant stirring, in order to promote polymerization of the citrate, through the polyesterification reaction. The molar ratio between citric acid and ethylene glycol used was set to 60/40 (mass ratio). After 4 h, water was completely removed, thereby yielding a translucent resin. Various (1, 2, 4 and 8 mol % of RE) dopant concentrations were considered. This percentage of RE is on the contribution of all dopants, such as: ZrO_2: 1%RE, ZrO_2: 2%RE, ZrO_2: 4%RE and ZrO_2: 8%RE correspond respectively to $Zr_{0.99}O_2$: $_{0.0033}$ Tb $_{0.0033}$ Tm $_{0.0034}$ Eu, $Zr_{0.98}O_2$: $_{0.0066}$ Tb $_{0.0066}$ Tm $_{0.0068}$ Eu, $Zr_{0.96}O_2$: $_{0.0133}$ Tb $_{0.0133}$ Tm $_{0.0134}$ Eu and $Zr_{0.92}O_2$: $_{0.0266}$ Tb $_{0.0266}$ Tm $_{0.0268}$ Eu. The polymeric resin was heat-treated at 350 ºC (10 ºC/ min) for 4 h, leading to partial decomposition of the polymeric gel; this resulted in the formation of an expanded resin, which consisted of partially pyrolyzed material. The resulting powders were annealed at 600 ºC for 2 h at a heating rate of 10 ºC/min.

2.2 Characterization of ZrO_2:RE (RE= Tm^{3+}, Tb^{3+}, and Eu^{3+}) powders

The as-synthetized powders were examined by XRD (Shimadzu diffractometer model XRD–7000), using Cu-Kα radiation. In addition, Raman spectrometry (Horiba

Jobin-Yvon Raman Labram) was performed at room temperature; an Olympus BX41 TM microscope equipped with a 514 nm-wavelength laser, was used as the excitation source. UV-vis reflectance spectra (Cary model 5G) and PL spectra (Thermal Jarrel-AshMonospec 27 monochromator and Hamatsu R446 photomultiplier) of the ZrO_2:RE particles were also obtained. A 350.7 nm-wavelength laser with krypton ions (CoherentInnova) and an output of ~13.3 mW, was used as the excitation source during the PL measurements; these measurements were all performed at room temperature. To characterize white light resulting from the aforementioned mixing, we calculated the chromaticity coordinates using the spectrum represented in Fig. 3. The chromaticity coordinates of red (the *x* coordinate), green (the *y* coordinate) and blue (the *z* coordinate) were determined according to the system of the International Commission on Illumination given in 1968 [41, 42] using the following relationships:

$$x = \frac{(X)}{(X+Y+Z)} \qquad y = \frac{(Y)}{(X+Y+Z)} \qquad z = \frac{(Z)}{(X+Y+Z)} \tag{1}$$

where parameters X, Y and Z are the following spectral integrals:

$$\mathrm{X} = \int \boldsymbol{x} P(\lambda) d\lambda \quad \mathrm{Y} = \int \boldsymbol{y} P(\lambda) d\lambda \quad Z = \int \boldsymbol{z} P(\lambda) d\lambda \tag{2}$$

Here P(λ) is luminescence spectrum of the samples, that provide, for each within the visible range , the emitted intensity. The function P(λ) is determined empirically, the values of λ for components *x*, *y* and *z* are 599, 555 and 446 nm, respectively and ***x***, ***y*** and ***z*** are functions of spectral summarizing. Integrals (2) were calculated through the spectral interval of 350-800 nm. The CCT value was estimated by using McCamy empirical formula [43]. The quality of white light is calculated using McCamy empirical formula in terms of CCT values, which is expressed as:

$$CCT = -449n^3 + 3525n^2 - 6823n + 5520.33 \tag{3}$$

where $n = \frac{(x-xe)}{(y-ye)}$ is the inverse slope line, *xe* = 0.332 and *ye* = 0.186

2.3 Computational details

First-principle calculations, based on the density functional theory (DFT), were performed by using the Vienna *ab initio* simulation package (VASP). The Kohn-Sham

equations were solved by using the Perdew, Burke, and Ernzerhof (PBE) exchange-correlation functional [44], and the electron-ion interaction was described via the projector-augmented-wave pseudo potentials. Moreover, the plane-wave expansion was truncated at a cut-off energy of 520 eV, and the Brillouin zones were sampled by using Monkhorst-Pack special k-point grids. Cubic and tetragonal phases of ZrO_2, both undoped and doped at 12% of Eu substituted for Zr, were considered. **In addition, a 12% of Tb and Tm substitutions were tested. The valence electron density is defined by 12 ($4s^2 4p^6 5s^2 4d^2$) electrons for Zr atoms, 6 ($2s^2 2p^4$) electrons for O atoms and 17 ($5s^2 5p^6 6s^2 4f^7$) electrons for Eu atoms. For Tb and Tm atoms, three f-like electrons are treated as core states and 9 electrons are used as valence states for both.**

A supercell with 48 atoms was used for both systems, 2 × 2 × 1 and 2 × 2 × 2 for cubic and tetragonal phases, respectively. In the case of 12% doping, two Zr^{4+} were substituted by two Eu^{3+} and oxygen vacancy (both near and far from Eu atoms) was included, to maintain the electroneutrality of the cell. In order to obtain a small amount of Eu doping, extremely large supercells must be used, thereby resulting in a high computational cost. The cell parameters and positions of all atoms were allowed to relax, and the conjugated gradient energy minimization method was used to obtain relaxed systems. This was achieved by setting a threshold value (i.e., 0.01 $eV \cdot Å^{-1}$) for the forces experienced by each atom. To ensure geometrical and energetic convergence of the cubic and tetragonal ZrO_2 structures, a 3 × 3 × 1 Monkhorst-Pack special k-point grid was used.

3. Results and discussion

3.1 XRD characterization

XRD patterns of pure ZrO_2 and co-doped ZrO_2:xRE (x = 1, 2, and 4%) powders are shown in Fig. 1(a)–(d). Diffraction peaks are located at approximate angles of: 30.07º, 35.02º, 50.28º, 59.87º, 62.60º, and 73.66º corresponding to the (101), (110), (112), (201), (103), and (202) planes, respectively, of the ZrO_2 tetragonal phase [ICSD 81-1546]. Fig. 1(e) shows the pattern corresponding to ZrO_2:8%RE. In this case, peaks occur at ~29.79°, 34.57°, 50.02°, 59.56°, 62.27°, and 73.35º, corresponding to the (111),

(200), (220), (311), (222), and (400) planes, respectively, of the cubic phase of ZrO_2 [ICSD 81-1551]. This phase is stabilized with increasing amount of bi- or trivalent cations introduced into the ZrO_2 structure [45, 46]. In addition, the replacement of Zr^{4+} cations by RE^{3+} results in the formation of oxygen vacancies. This leads, in turn, to a change in the lattice parameters of the unit cell ($c/a \rightarrow 1$) and consequently, arrangement of the ions in a cubic structure [46]. The ionic radius of oxygen is large, it becomes difficult to maintain the four O^{2-} ions around an ion Zr^{4+} with a fluorite structure (cubic), due to large repulsion between the ions O^{2-}. With the introduction of dopant RE^{3+} replacing Zr^{4+}, there is the appearance of oxygen vacancies in order to offset the charges and as result the force of repulsion between the O^{2-} decreases, giving conditions to accommodate the ions in the cubic structure.

INSERT FIGURE 1

The size of the crystallites in the sample was estimated from the Scherrer equation [47, 48] and the full-width half-maximum (FWHM) of an observed peak. The average crystallite size (D) of ZrO_2:RE powders was determined from the strongest peaks corresponding to the (101) tetragonal phase and (111) cubic phase. The lattice parameter (a, c), unit-cell volume (V), and crystallite size of the ZrO_2:RE samples are listed in Table 1.

INSERT TABLE 1

3.2 Raman characterization

ZrO_2 polymorphism may lead to inaccurate results when the crystalline phases of ZrO_2 are identified only via XRD. Das et al. [45] attributed inaccuracies in XRD identification of tetragonal and cubic phases, to the low angular resolution (0.03º) of the equipment used; this resolution resulted in an overlap of the peaks corresponding to these phases. Compared to XRD, Raman spectroscopy can more accurately distinguish among the crystalline phases of ZrO_2 [49]. The band positions, intensities, and shapes can be determined from the Raman spectra. In fact, as shown in Fig. 2 and Table 2, each

structure exhibits certain characteristics that correspond to specific locations in the spectra.

INSERT FIGURE 2

The bands that occur at 142, 257, 314, 461, 609, and 627 cm^{-1} in the spectra shown in Fig. 2(a), (b), and (c) are attributed to the vibration modes of tetragonal ZrO_2 [49–51]. The spectrum (d) of the cubic phase of ZrO_2 (fluorite) is characterized by a broad band that occurs at ~605 cm^{-1} [49]. The active modes in the Raman spectra (corresponding to each crystal) and the c/a ratio of the lattice parameters of tetragonal zirconia, are shown in Table 2. Theoretical calculations of the Raman-active modes of pure tetragonal ZrO_2 yield values of 149.4, 294.2, 301.5, 453.6, 611.5, and 650.9 cm^{-1} for the E_g, A_{1g}, B_{1g}, E_g, B_{1g}, and E_g modes, respectively. In the case of pure cubic ZrO_2, a unique mode, which has T_{2g} symmetry, occurs at a wavenumber of 600.7 cm^{-1}. These values concur with previously obtained experimental data.

INSERT TABLE 2

3.3 UV–Visible spectroscopy analysis

The band gap energies of the ZrO_2:RE nanoparticles were estimated from the respective diffuse-reflectance spectra, by plotting the square of the Kubelka–Munk function (i.e., $F(R)^2$) as a function of the energy (in eV). The values were determined by extrapolating the linear part of the curve to $F(R)^2 = 0$, as shown in Fig. 3. The ratio between the molar absorption coefficient (k) and scattering coefficient (s) is estimated from reflectance data using the Kubelka–Munk relation [52] in equation 4:

$$F(R) = \frac{k}{s} = \frac{(1-R)^2}{2R} \qquad (4)$$

where R is the percentage of reflected light. The incident photon energy ($h\nu$) and the optical band gap energy (E_g) are related to the transformed Kubelka–Munk function, $[F(R)\ h\nu]^p = A(h\nu - Eg)$, where E_g is the band gap energy, A is a constant depending on the transition probability and p is the power index that is related to the optical

absorption process. p equals to 1/2 or 2 for an indirect or a direct allowed transition, respectively.

INSERT FIGURE 3

The E_g values are shown in Fig. 3. Intermediate levels of energy in the band gap region result from the structural defects in ZrO_2 [53]. For example, oxygen vacancies, the type of structural defect that occurs in the present case, are generated in order to compensate for the Zr^{4+} ions replaced by RE^{3+} ions. E_g values of 5.21, 5.09, 5.06, 4.97, and 4.92 eV are obtained for the undoped, 1, 2, 4, and 8 mol.% RE-doped materials, respectively.

In addition, the calculated values of the cell parameters concur with the experimentally determined results (a = 5.127 Å for the cubic phase, and a = 3.630 Å and c = 5.264 Å for the tetragonal phase). The results of the theoretical calculations indicate that, in both the cubic and tetragonal structures, 12% of Eu produces a local distortion that is both centered on the dopant, and located near the oxygen vacancy (Vo). The geometry of doped ZrO_2 with Eu^{+3} showing the coordination polyhedra of the cubic and tetragonal phases is shown in Fig. 4.

INSERT FIGURE 4

The vacancy corresponding to an O atom missing from the structure was examined by taking into account the proximity of the Eu atoms. For both phases, large distances between the oxygen vacancy and the Eu atoms, constitute more favorable arrangements than other configurations. Consequently, some Zr atoms are seven-coordinated in the case of the cubic phase and are also neighbored by an Eu atom in the case of the tetragonal phase (see Table 3).

INSERT TABLE 3

The difference between the formation energies of the cubic and tetragonal phases (ΔE_{C-T}) of ZrO_2 and $Zr_{0.88}Eu_{0.12}O_{1.94}$ are 0.84 eV and -0.34 eV, respectively. These results indicate that the incorporation of Eu into the ZrO_2 structure increases the already higher stability of the cubic phase, relative to that of the tetragonal phase. This explains the preferential Eu doping of the cubic phase of the films.

We used a supercell model in which the cubic and tetragonal phases are each assigned 48 atoms, to determine the effect of Eu incorporation into the ZrO_2 lattice, on the electronic structure. The total and projected density of states (DOS) of the atoms and orbitals of the pure and doped cubic phase are shown in Fig. 5; the results corresponding to the pure and doped tetragonal phase are shown in Fig. 6.

INSERT FIGURE 5

INSERT FIGURE 6

The top of the VB and the bottom of the conduction band (CB) are composed mainly of O 2p levels and Zr 4d levels, respectively. Furthermore, E_g values of 3.21 eV and 3.83 eV were calculated for the respective undoped cubic and undoped tetragonal phases. These values are both lower than their experimentally determined counterparts. However, compared to the former (3.21 eV), the latter (3.83 eV) is closer to E_g of the pure ZrO_2 (5.21 eV), investigated in this work. A comparison of the electronic structures shown in Figs. 5(b) **and 6(b)** reveals that Eu doping leads to a systematic decrease in E_g and an increase in the density of electronic states inside the gap. **Moreover, the effect of Tb and Tm incorporation into the ZrO_2 lattice has been also explored, and the total and projected density of states on atoms for doped Tb and Tm, in cubic and tetragonal phases, are shown in Fig. S1 of supplementary information. Therefore, the theoretical calculations indicate that these states occur in the forbidden zone of energy, owing to the presence of Eu, Tb and Tm transition metals and O vacancies in the ZrO_2 lattice.**

3.4 PL studies

The optical properties of Eu dopants in various host materials, have been characterized [54–62]. Owing to the hypersensitivity of the $^5D_0 \rightarrow {}^7F_2$ transition, Eu ions can be used to monitor morphological changes in the host material, which are induced by external stimuli [63–66].

Figure 7 shows the PL spectra of both the undoped and co-doped ZrO_2. The band in the emission spectrum of undoped ZrO_2 ranges from 376 nm–648 nm with a peak centered at 460 nm, as shown in Fig. 7. This is attributed to the (O^{2-}) p → d (Zr^{4+})-type transition [53], which results from a sequence of non-radiative relaxations of

localized electrons in the CB; this is followed by band recombination within the band gap, and subsequent decrease in energy of the electrons when they move to the VB [67]. Factors such as the particle size and morphology, crystallinity, and the method of synthesis [68–69] may influence the photoluminescent properties of the zirconia.

INSERT FIGURE 7

The PL spectra of ZrO_2:RE (RE=Tm^{3+}, Tb^{3+}, and Eu^{3+}) powders exhibit characteristics of each dopant-ion emission. For example, in the case of excitation at 350 nm, the emission peak at 477 nm is attributed to Tm^{3+}, which is associated with the $^1G_4 \rightarrow {}^3H_6$ transition [70, 71]. The $^5D_4 \rightarrow {}^7F_6$ and $^5D_4 \rightarrow {}^7F_5$ transitions occur at wavelengths of 496.02 nm and 548.32 nm, respectively, and are associated with the emission of Tb^{3+} [72, 73]. In addition, the Eu^{3+}, $^5D_0 \rightarrow {}^7F_1$, and $^5D_0 \rightarrow {}^7F_2$ transitions occur at respective wavelengths of 597.16 nm and 617.54 nm [74, 75]. The interference of the host has a more significant effect on the photoluminescent behavior of ZrO_2:8%RE than on the behavior of ZrO_2. This effect is manifested as the occurrence of a broad band at wavelengths ranging from 380 nm–480 nm, and results from the structural defects in ZrO_2. **The order-disorder effects in the coordination of some Zr and doped atoms, verified by theoretical calculations, can result in the production of new levels between the valence and the conduction bands, which favor the PL emission properties.** As Fig. 7(c) shows, the emission intensity of the Eu^{3+} ions increases with increasing concentration of Eu^{3+}, reaches a maximum at 4 mol.% RE, and decreases thereafter (owing to the quenching effect) [76]. The critical quenching concentration of Eu^{3+} is defined as the concentration at which the emission intensity begins to decrease. Similarly, the critical distance, corresponding to the critical quenching concentration, is defined as the average distance between the nearest Eu^{3+} ions, at which energy transfer processes occur.

3.5 Energy transfer in ZrO_2:RE (RE=Tm^{3+}, Tb^{3+}, and Eu^{3+}) powders

A schematic energy level diagram illustrating Tm^{3+}, Tb^{3+}, and Eu^{3+} absorption, non-radiative relaxation, and processes leading to blue, green, and red emissions is shown in Fig. 8. **The energy level $^5D_4$ of Tb^{3+} is very close to the energy**

level of Tm^{3+} $^1G_4$ as seen in the energy diagram (Figure 8). This setting energy levels contributes to efficient energy transfer process (ET1) between Tm^{3+} ions and Tb^{3+} [77]. The $^1G_4$ level of Tm^{3+} is completely filled by the charge carriers (electrons) from the excitation process (λ = 350 nm). The increased concentration of Tm^{3+} promotes the increase of the intensity of the transition $^1G_4 \rightarrow {}^3H_6$, this increased intensity of Tm^{3+} also acts as a source for transporting energy for the sublevel $^5D_4$ of Tb^{3+}, this effect is realized by increasing the intensity of transition $^5D_4 \rightarrow {}^7F_5$ (550 nm) Tb^{3+}, shown in Figure 7.

The Energy transfer (ET2) between Tb^{3+} and Eu^{3+} has been extensively studied, in order to understand the photoluminescent behavior [78]. In fact, the luminescence intensities of various rare-earth ions can be enhanced or quenched by the energy transfer from other co-doped rare-earth ions [79–81]. ET2 between Tb^{3+} and Eu^{3+} may occur in hosts, such as tungstates, zeolite-Y, yttria, porous silicon, borate, hydrate, and molybdates [82–85]. The probability of this transfer is proportional to R^{-6} (R: average distance between Tb^{3+} and Eu^{3+}), and hence the efficiency of the ET2 process increases gradually with increasing Eu^{3+}-doping concentration. Furthermore, R decreases with increasing Eu^{3+} concentration and therefore, the energy transfer efficiency of $Tb^{3+} \rightarrow Eu^{3+}$ increases. Owing to the quenching effect, this behavior is not unique to the ZrO_2:8% RE, as shown in Fig. 7(c).

INSERT FIGURE 8

An analysis of the results depicted in Fig.8 renders that electrons on Tb^{3+} ions are promoted from the ground state ($4f^8$) to the excited state ($4f^75d$), by 350.7-nm UV light. These electrons then relax to the lowest excited state $^5D_4$, by means of a multi-phonon relaxation process. The electrons may return to the ground state, thereby resulting in Tb^{3+} emissions ($^5D_4 \rightarrow {}^7F_{6,\,5,\,4}$). Alternatively, their excitation energy may be transferred from the $^5D_4$ (Tb^{3+}) level to the higher excited energy levels of Eu^{3+} ($4f^6$) through cross relaxation; these levels then relax to the $^5D_0$ (Eu^{3+}) level, thereby resulting in red-orange emissions ($^5D_0 \rightarrow {}^7F_{0,\,1,\,2}$). The $^5D_4 \rightarrow {}^7F_{6,\,5,\,4,\,3}$ emissions of Tb^{3+} overlap with the $^7F_{0,\,1} \rightarrow {}^5D_{0,\,1,\,2}$ absorptions of Eu^{3+} and hence, the energy transfer from Tb^{3+} to Eu^{3+} is, in general, very efficient.

Fig. 9 shows the CIE coordinates of ZrO_2:xRE (1–8 mol.%), while Table 4 lists the CIE coordinate values and CCT values for samples ZrO_2:xRE (1–8 mol.%). We

obtained white light emission from a single component, by co-doping the ZrO_2 host with Tm^{3+}, Tb^{3+}, and Eu^{3+} ions. Under the excitation of UV light, a full-color emission is obtained, resulting from the simultaneous blue, green, and red emission of the Tm^{3+}, Tb^{3+}, and Eu^{3+} ions. **It is observed in Figure 7, for the sample ZrO_2: 8% RE, the photoluminescent behavior of ZrO_2 host was very significant. The presence of oxygen vacancies (V_0) in the matrix is responsible for the emergence of broadband emission at around 450 nm [86]. The oxygen vacancy always leads to formation of energy levels within the band gap. When ZrO_2 is excited by a photon, the electrons are trapped by V_0 and centers are created (F) [87]. Then recombination centers (F) with the holes (h^+) creates the transmitter excited states. From these states originate transitions which decay to a state with lower energy level. The band of blue emission from the ZrO_2 contributes along with the specific emission of rare earth on white emission as shown in Figure 8. A** single-composition white-emitting phosphor is therefore obtained. In fact, this white emission occurs independent of the excitation, depends on the doping concentration of the rare-earth ions, and is obtained by blending the aforementioned simultaneous emissions. The emissions are characterized by the colors emitted from each sample. This characteristic is defined by chromaticity coordinates *x* and *y*.

INSERT FIGURE 9

INSERT TABLE 4

4. Conclusions

ZrO_2:RE powders were successfully obtained via complex polymerization. The phase (i.e., tetragonal) comprising the ZrO_2:xRE (x: 1, 2, and 4 mol.%) samples was identified via XRD analysis, whereas the cubic phase, stabilized in ZrO_2:8%RE, was identified via Raman spectroscopy. The structural and electronic effects, resulting from Eu in both the cubic and tetragonal ZrO_2:Eu^{3+} phases, were explained by calculating (using DFT) the relevant energies. The photoluminescence emission spectra reveal transitions of the type: $^1G_4 \rightarrow {}^3H_6$ (477 nm), $^5D_4 \rightarrow {}^7F_{5,6}$ (496.02 nm and 548.32 nm), and $^5D_0 \rightarrow {}^7F_{1,2}$ (597.16 nm and 617.54 nm) from Tm^{3+}, Tb^{3+}, and Eu^{3+}, respectively. An inter-level energy transfer, $^5D_4$ (Tb^{3+}) $\rightarrow$ $^5D_1$ (Eu^{3+}), also occurred. In

addition, according to the CIE diagram, the CIE coordinates (x: 0.34 and y: 0.34) calculated for ZrO_2: 8%RE, correspond to a point that lies in the white region. The results of this work suggest that these materials have significant potential for use in the field of light-emitting diodes.

Acknowledgment

The authors gratefully acknowledge the financial support of the Brazilian governmental research funding agencies CAPES, CNPq, FAPESP 2013/07296-2 and INCTMN 2008/57872-1.

References

1. F. Auzel, *Upconversion and anti-Stokes processes with f and d ions in solids,* Chem. Rev, 104 (2004) 139−174.
2. J.-C.G. Bunzli, *Benefiting from the Unique Properties of Lanthanide Ions,* Acc. Chem. Res., 39 (2006) 53-61.
3. R. Bazzi et al., *Synthesis and luminescent properties of sub-5-nm lanthanide oxides nanoparticles,* Journal of Luminescence, 102-103 (2003) 445-450.
4. S. M. Hussain, A. M. Schrand, R. C. Murdock, D. M. Mattie, J. J. Schlager and M. Terrones, *Toxicity evaluation for safe use of nanomaterials: recent achievements and technical challenges* Adv. Mater., 21 (2009) 1549-155.
5. F. T. Wang, Y. Zhang, X. Fan, M. Wang, *Luminescent nanomaterials for biological labelling, Nanotechnology.* 17 (2006) R1-R17.
6. F. L. Wang et al., *Recent advances in the chemistry of lanthanide doped upconversion nanocrystals,* Chem. Soc. Rev, 38 (2009) 976−989.

7. F. Wang, D. Banerjee, L. Yonqshenq, X. Chen, X. Liu, *Upconversion nanoparticles in biological labeling, imaging, and therapy*, Analyst, 135 (2010) 1839-1854.

8. J. S. Shen, C. Yan, *Luminescent rare earth nanomaterials for bioprobe applications.* Dalton Trans., 48 (2008) 5687-5697.

9. J. L. Zhou, F. Li, *Upconversion nanophosphors for smalanimal imaging*, Chem. Soc. Rev., 41 (2012) 1323−1349.

10. D.E.A. Achatz, O. S. Wolfbeis, *Luminescent chemical sensing, biosensing, and screening using upconverting nanoparticles.* Top. Curr. Chem., 300 (2011) 29-50.

11. M. Haase, H. Schafer, *Upconverting nanoparticles.* Angew. Chem., Int. Ed. , 50 (2011) 5808-5829.

12. Y. Yang, *Upconversion nanophosphors for use in bioimaging, therapy, drug delivery and bioassays.* Microchim Acta 181 (2014) 263-294.

13. H. K. Kobayashi, M. Ogawa, N. Y. Morgan, P. D. Smith, C. B. Murray, X. Ye, J. Collins, G. A. Kumar, H. Bell, P. L. Choyke, *In vivo multiple color lymphatic imaging using upconverting nanocrystals.* J. Mater. Chem., 19 (2009) 6481-6484.

14. S. H. Wu, D. J. Milliron, S. Aloni, V. Altoe, D. V. Talapin, B. E. Cohen, P. J, Schuck, *Non-blinking and photostable upconverted luminescence from single lanthanide-doped nanocrystals.* Natl. Acad. Sci. U.S.A., 106 (2009) 10917-10921.

15. S. Mukherjee, D. P. Dutta, N. Manoj, A. K. Tyagi, *Sonochemically synthesized rare earth double-doped zirconia nanoparticles: probable candidate for white light emission*, J Nanopart Res 14 (2012) 814.

16. W. Du, Z. Zhu, X. Zhang, D. Wang, D. Liu, X. Qian, and J. Du, *RE/ZrO_2 (RE = Sm, Eu) composite oxide nano-materials: Synthesis and applications in photocatalysis.* Mater. Res. Bull. 48 (2013) 3735–3742.

17. R. Marin, G. Sponchia, E. Zucchetta, P. Riello, G. De Portu, F. Enrichi, and A. Benedetti, *Monitoring the t → m Martensitic Phase Transformation by Photoluminescence Emission in Eu^{3+}-Doped Zirconia Powders.* J. Am. Ceram. Soc. 96 (2013) 2628–2635.

18. A. Speghini, P. Riello, S. Bucella, and A. Benedetti, *Preparation, structural characterization, and luminescence properties of Eu^{3+}-doped nanocrystalline ZrO_2*. J. Mater. Res, 20 (2005) 2780-2791.

19. E. De la Rosa, P. Salas, R. A. Rodríguez, *Visible light emission under UV and IR excitation of rare earth doped ZrO_2 nanophosphor.* Opt. Mater., 27 (2005) 1320-1325.

20. G. García-Rosales et al., *Energy transfer from Tb^{3+} to Eu^{3+} ions sorbed on $SrTiO_3$ surface*. Journal of Luminescence, 132 (2012) 1299-1306.

21. S. Gai, C. Li, P. Yang, and J. Lin, *Recent Progress in Rare Earth Micro/Nanocrystals: Soft Chemical Synthesis, Luminescent Properties, and Biomedical Applications*, Chem. Rev., 114 (2014) 2343-2389.

22. Z. W. Quan, J. Lin, *Synthesis and characterization of spherical ZrO_2: Eu^{3+} phosphors by spray pyrolysis process.* Mater. Res. Bull, 40 (2005) 810-820.

23. A. Gedanken, E. Sominski, O. Palchik, Y. Koltypin, G. Panczer, M. Gaft, and H. Minti, *Sonochemical Preparation and Characterization of Europium Oxide Doped In and Coated On ZrO_2 and Yttrium-Stabilized Zirconium (YSZ).* J. Phys. Chem. B 104 (2000) 7057–7065

24. N. Tiwari,S. R. Kuraria, *Effect of variable trivalent europium concentration on photo- and thermoluminescence of zirconium dioxide nanophosphors.* Materials Science in Semiconductor Processing, 31 (2015) 214-222.

25. M. García-Hipólito,O. Álvarez-Fregoso, C. Falcony, M. A. Aguilar-Frutis, *Preparation and characterization of Eu doped zirconia luminescent films synthesized by pyrosol technique.* J. Mater. Sci. Lett., 20 (2001) (1799-1801).

26. E. Pereyra-Perea, M. García, *Preliminary studies on luminescent terbium doped ZrO2 thin films prepared by sol-gel process.* Phys. D: Appl. Phys., 31 (1998) L7–L10.

27. H. Zhang, S. Niu, and Q. Xin, *Blue emission of ZrO_2:Tm nanocrystals with different crystal structure under UV excitation.* J. Non-Cryst. Solids 354 (2008) 1559-1563.

28. Y. S. Vidya et al., *Phase transformation of $ZrO_2:Tb^{3+}$ nanophosphor: Color tunable photoluminescence and photocatalytic activities.* Journal of Alloys and Compounds, 622 (2015) 86-96.

29. B. Marí et al., *Preparation and luminescence properties of Tb^{3+} doped ZrO_2 and $BaZrO_3$ phosphors.* Journal of Luminescence, 130 (2010) 2128-2132.

30. M. Shang, X. Kang, D. Yang, Y. Zhang, and J. Lin, *Hydrothermal Derived $LaOF:Ln^{3+}$ (Ln = Eu, Tb, Sm, Dy, Tm, and/or Ho) Nanocrystals with Multicolor-Tunable Emission Properties.* Inorg. Chem., 51 (2012) 11106−11116.

31. B. C. Joshi, *Enhanced Eu^{3+} emission by non-radiative energy transfer from Tb^{3+} in zinc phosphate glass.* Journal of Non-Crystalline Solids, 180 (1995) 217-220.

32. S.-H. Yang et al., *Luminescence of CNT coated $LaPO_4$:Tm phosphors and their field emission lamp application.* Journal of Alloys and Compounds, 612 (2014) 210-214.

33. A. A. Ansari et al., *Structural and photoluminescence properties of Tb-doped $CaMoO_4$ nanoparticles with sequential surface coatings.* Materials Chemistry and Physics, 147 (2014) 715-721.

34. X. Zhou et al., *$LiY_{1-x}Eu_x(MoO_4)_2$ as a promising red-emitting phosphor of WLEDs synthesized by sol-gel process.* Journal of Rare Earths, 30 (2012) 315-319.

35. J. C. Zhang et al., *White light emitting glasses.* Journal of Solid State Chemistry, 93 (1991) 17-29.

36. C. Zhu et al., *Luminescence properties of Tb doped and Tm/Tb/Sm co-doped glasses for LED applications.* Journal of Luminescence, 130 (2010) 74-77.

37. P. N. Medeiros, A. P. Marques, R. L. Tranquilin, C. A. Paskocimas, M. R. D. Bomio, J. A.Varela, E. Longo and F. V. Motta, *Effect of different starting materials on the synthesis of $Ba_{0.8}Ca_{0.2}TiO_3$.* Journal of Advanced Ceramics 65 (2015)65.

38. V. D. Araujo, F. V. Motta., A. P. Marques, Effect of calcium on the structural properties of $Ba_{(1-x)}Ca_xTiO_3$ particles synthesized by complex polymerization method. J Mater Sci 49 (2014) 2875.

39. F. V. Motta, A. P. Marques, J. W. M. Espinosa, P. S. Pizani, E. Longo, J. A. Varela, Room temperature photoluminescence of BCT prepared by Complex Polymerization Method. Current Applied Physics, 10 (2010) 16.

40. T. M. Mazzo el at., Photoluminescence properties of $CaTiO_3:Eu^{3+}$ nanophosphor obtained by the polymeric precursor method. Materials Chemistry and Physics, 145 (2014) 141.

41. E. F. Schubert, Light Emitting Diodes, Cambridge University Press, 2003.

42. R. Robertson, Computation of correlated color temperature and distribution temperature, J. Opt. Soc. Am. 58 (1968)1528.

43. C. S. McCamy. Correlated color temperature as an explicit function of chromaticity coordinates, Wappingers Falls, New York 12590- 1804.

44. J. P. Perdew and K. Burke, *Rationale for mixing exact exchange with density functional approximations.* Journal of Chemical Physics, 105 (1996) 9982-9985.

45. S. Das et al., *Structural and Optical Properties of Tunable Warm-White Light-Emitting $ZrO_2:Dy^{3+}$–Eu^{3+} Nanocrystals.* J. Am. Ceram. Soc., 96 (2013) 1602-1609.

46. N. Shibata, A. Kuwabara, Y. Ikuhara, T. Sakuma, *The instability and resulting phase transition of cubic zirconia.* Materials Science and Engineering A, 302 (2001) 90-98.

47. H. P. Klug, *X-ray Diffraction Procedures for Polycrystalline and Amorphous Materials.* John Wiley & Sons, New York, 1962, p.p. 491-538.

48. E. W. Nuffield, *Diffraction Procedures Methods.* John Wiley and Sons, New York, 1986,p.p. 147-148.

49. C. G. Kontoyannis, *Quantitative determination of the cubic, tetragonal and monoclinic phases in partially stabilized zirconias by Raman spectroscopy.* Journal of materials science 29 (1994) 5316-5320.

50. D. Bersani et al., *Micro-Raman study of indium doped zirconia obtained by sol–gel.* Journal of Non-Crystalline Solids, **345–346**(2004) 116-119.

51. C. Wulfman, M. Sadoun and M. Lamy de la Chapelle, *Interest of Raman spectroscopy for the study of dental material: The zirconia material example.* IRBM, 31(2010) 257-262.

52. P. Kubelka, F. Munk-Aussig, *Ein beitrag zur optick der farbanstriche*, Zeitschrift fur technische, Physik, 12 (1931) 593-601.

53. M. D. Gonçalves et al., *(Sr,Tm)ZrO_3 powders prepared by the polymeric precursor method: Synthesis, optical properties and morphological characteristics.* Optical Materials, 31 (2009) 1134-1143.

54. B. Bihari, H. Eilers and B.M. Tissue, *Spectra and dynamics of monoclinic Eu_2O_3 and Eu^{3+}:Y_2O_3 nanocrystals.* Journal of Luminescence, 75 (1997) 1-10.

55. R. Debnath, A. Nayak, and A. Ghosh, *On the enhancement of luminescence efficiency of Y_2O_3:Eu^{3+} red phosphor by incorporating (Al^{3+}, B^{3+}) in the host lattice.* Chemical Physics Letters, 444 (2007) 324-327.

56. H. Eilers and B. M. Tissue, *Laser spectroscopy of nanocrystalline Eu_2O_3 and Eu^{3+}:Y_2O_3.* Chemical Physics Letters, 251 (1996) 74-78.

57. X. R. Z. Hou, Y. K. Li, W. J. Li, *Luminescent properties of nano-sized Y_2O_3:Eu fabricated by co-precipitation method* J Alloy Compd, 494 (2010) 382.

58. J. Guohua, *Local Site Symmetry Determination of Scheelite-Type Structures by Eu^{3+} Spectroscopy.* J. Phys. Chem. C, 114 (2010) 17905–17913.

59. M. Jia et al., *UV excitation properties of Eu^{3+} at the S6 site in bulk and nanocrystalline cubic Y_2O_3.* Chemical Physics Letters, 384 (2004) 193-196.

60. X. Qu, B. K. Moon, B. C. Choi, J. H. Jeong and K. H. Kim, *Preparation and Photoluminescence Properties of $Gd_2O_3:Eu^{3+}$ Inverse Opal Photonic Crystals.* J Phys Chem C 114 (2010) 19891.

61. C. Shang, X. Shang, M. Li, and L. Zhao, *Investigation on the Luminescence Improvement of Nanosized La_2O_3/Eu^{3+} Phosphor under Charge-Transfer Excitation.* J. Phys. Chem. C 115 (2011) 2630–2635.

62. C. Shang et al., *Investigation on the red shift of charge transfer excitation spectra for nano-sized $Y_2O_3:Eu^{3+}$*. Chemical Physics Letters, 501 (2011) 480-484.

63. K. Binnemans, *Lanthanide-Based Luminescent Hybrid Materials.* Chem. Rev., 109 (2009) 4283-4374.

64. K. Binnemans and C. Görller-Walrand, *A simple model for crystal field splittings of the $^7F_1$ and $^5D_1$ energy levels of Eu^{3+}*. Chemical Physics Letters, 245 (1995) 75-78.

65. G. Blasse, *The Eu^{3+} luminescence as a measure for chemical bond differences in solids.* Chem. Phys. Lett., 20 (1973) 573.

66. T. Myint and H. Eilers, *Light-induced structural changes in Eu-doped $(Pb,La)(Zr,Ti)O_3$ ceramics.* Appl. Phys. Lett., 98 (2011) 171906.

67. J. Liang, X. Jiang, Y. Li, *Photoluminescence of Tetragonal ZrO_2 Nanoparticles Synthesized by Microwave Irradiation.* Inorg Chem 41 (2002) 3602.

68. L. J. Lai, H. K. Chen, M. B. Cheng, M. I. Lin, and T. C. Chun, *Photoluminescence of zirconia films with VUV excitation.* Journal Electron Spectroscopy Related Phenomena, 865 (2005) 144-147.

69. L. Kumari, J. M. Xu, R. M. Leblanc, D. Z. Wang, Y. Li, H. Guo, J. Zhang, *Controlled Hydrothermal Synthesis of Zirconium Oxide Nanostructures and Their Optical Properties.* CrystGrownth Des 9 (2009) 3874-3880.

70. J. W. Shur, K. H. Choi and D.H. Yoon, *Growth of Zr co-doped Tm:$LiNbO_3$ single crystal for improvement of photoluminescence property in blue wavelength range.* Journal of Crystal Growth, 318 (2011) 653-656.

71. H. Zhang et al., *Photoluminescence of YVO_4:Tm phosphor prepared by a polymerizable complex method.* Solid State Communications, 132 (2004) 527-531.

72. Y. Xie, L. Liu, Y. Su, H. Zhao, Y. Liu, Z. Zhang, H. Duan, J. Li, and E. Xie, *Oxygen defects-modulated green photoluminescence of Tb-doped ZrO_2 nanofibers.* Applied Physics Letters 97 (2010) 141916.

73. R. E. Muenchausen et al., *Effects of Tb doping on the photoluminescence of Y_2O_3:Tb nanophosphors.* Journal of Luminescence, 126 (2007) 838-842.

74. R. K. Tamrakar, D. P. Bisen, K. Upadhyay, *Photoluminescence behavior of ZrO2: Eu^{3+} with variable concentration of Eu^{3+} doped phosphor*, Journal of Radiation Research and Applied Sciences 8 (2015) 11-1675.

75. M. Najafi and H. Haratizadeh, *The effect of growth conditions and morphology on photoluminescence properties of Eu-doped ZnO nanostructures.* Solid State Sciences, 41 (2015) 48-51.

76. O. Meza, L. A. Diaz-Torres, H. Desirena, J. L. Rodríguez-Lopez, *Luminescence Concentration Quenching Mechanism in Gd2O3:Eu3+*. J. Phys. Chem. A 118 (2014) 1390-1396.

77. C.P. Wyss, M. Kehrli, Th. Huber, P.J. Morris, W. LuKthy, H.P. Weber, A.I. Zagumennyi, Y.D. Zavartsev, P.A. Studenikin, I.A. Shcherbakov, A.F. Zerrouk,

Excitation of the thulium $^1G_4$ level in various crystal hosts, Journal of Luminescence 82 (1999) 137-144.

78. T. K. Anh, N. Vu et al., , *Nanomaterials containing rare-earth ions Tb, Eu, Er and Yb: preparation, optical properties and application potential.* Journal of Luminescence, 102-103 (2003) 391-394.

79. G. Li, Z. Hou, C. Peng, Z. Cheng, and J. Lin, J., *Nanocrystalline LaOCl:Tb^{3+}/Sm^{3+} as promising phosphors for full-color field-emission displays.* Opt. Lett. 34 (2009) 3833-3835.

80. A. G. Macedo, D. Ananias, M. V. Reis, V. S. Amaral, L. D. Carlos and J. Rocha, *Effects of Phonon Confinement on Anomalous Thermalization, Energy Transfer, and Upconversion in Ln^{3+}-Doped Gd_2O_3 Nanotubes.* Advanced Functional Materials 20 (2010) 624-634.

81. B. H. Lee et al., *The effect to Tb^{3+} Co-doping on the photoluminescence of $(Sr,Ba)_2SiO_4:Eu^{2+}$*. J. Electrochem. Soc., 157 (2010) 227-232.

82. W. W. Holloway, M. Kestigian and R. Newman, *Direct Evidence for Energy Transfer Between Rare Earth Ions in Terbium-Europium Tungstates.* Physical Review Letters, 11 (1963) 458-460.

83. W. Chen, Y. Huang, *Photoluminescence and photostimulated luminescence of Tb^{3+} and Eu^{3+} in zeolite-Y.* Journal of Applied Physics 88 (2000) 1424-1431.

84. K. Anh et al., *Energy transfer between Tb^{3+} and Eu^{3+} in Y_2O_3 crystals.* Journal of Luminescence, 39 (1988) 215-221.

85. J. Yang, C. Li, Y. Yu, and Y. Lin, *Energy Transfer and Tunable Luminescence Properties of Eu^{3+} in $TbBO_3$ Microspheres via a Facile Hydrothermal Process.* Inorg. Chem., 47 (2008) 7262-7270.

86. C. Lin, C. Zhang and Jun Lin, Phase Transformation and Photoluminescence Properties of Nanocrystalline ZrO_2 Powders Prepared via the Pechini-type Sol-Gel Process, J. Phys. Chem. C 111 (2007) 3300-3307

87. A. A. Benyagoub, Mechanism of the monoclinic-to-tetragonal phase transition induced in zirconia and hafnia by swift heavy ions, Phys. Rev. B 72 (2005) 094114.

FIGURE CAPTIONS

Figure 1: XRD patterns of (a) non-doped ZrO_2 and ZrO_2:xRE (b) x = 1%, (c) x = 2%, (d) x = 4%, and (e) x = 8%, calcined at 600°C.

Figure 2: Raman spectrum of ZrO_2:xRE, (a) x = 1%, (b) x = 2%, (c) x = 4%, and (d) x = 8%.

Figure 3: UV-visible absorption spectra for particles: undoped ZrO_2 and ZrO_2:x% RE (x= 1, 2, 4, and 8% mol).

Figure 4: Geometry of doped ZrO2 with Eu^{3+} showing the coordination polyhedral: a) cubic phase and b) tetragonal phase.

Figure 5: Total and projected density of states on atoms and orbitals for the pure (a) and doped cubic phase (b).

Figure 6: Total and projected density of states on atoms and orbitals for the pure (a) and doped tetragonal phase (b).

Figure 7: Photoluminescence emission spectra of (a) ZrO_2:xRE (x = 1–8 mol%), (b) undoped ZrO_2, (c) quenching effect in the transition $^5D_0 \rightarrow {}^7F_1$ (Eu^{3+}) at 617.54 nm.

Figure 8: Schematic diagram of the Tm^{3+}, Tb^{3+}, and Eu^{3+} energy levels and the processes leading to blue, green, and red emission.

Figure 9: CIE chromaticity diagram for ZrO_2:xRE (x = 1, 2, 4, and 8 mol%).

TABLE CAPTIONS

Table 1 - Value of structural parameters of ZrO_2:xRE (x = 0–8 mol%) nanophosphors.

Table 2 – Active Raman modes, space group, and c/a lattice parameter ratio for the zirconia polymorphs.

Table 3: Distances in A for the coordination polyhedra for doped ZrO_2 with Eu^{3+} for the cubic and tetragonal phases.

Table 4 - Chromaticity coordinates for ZrO_2:xRE (x = 1, 2, 4, and 8 mol%).

graphical abstract

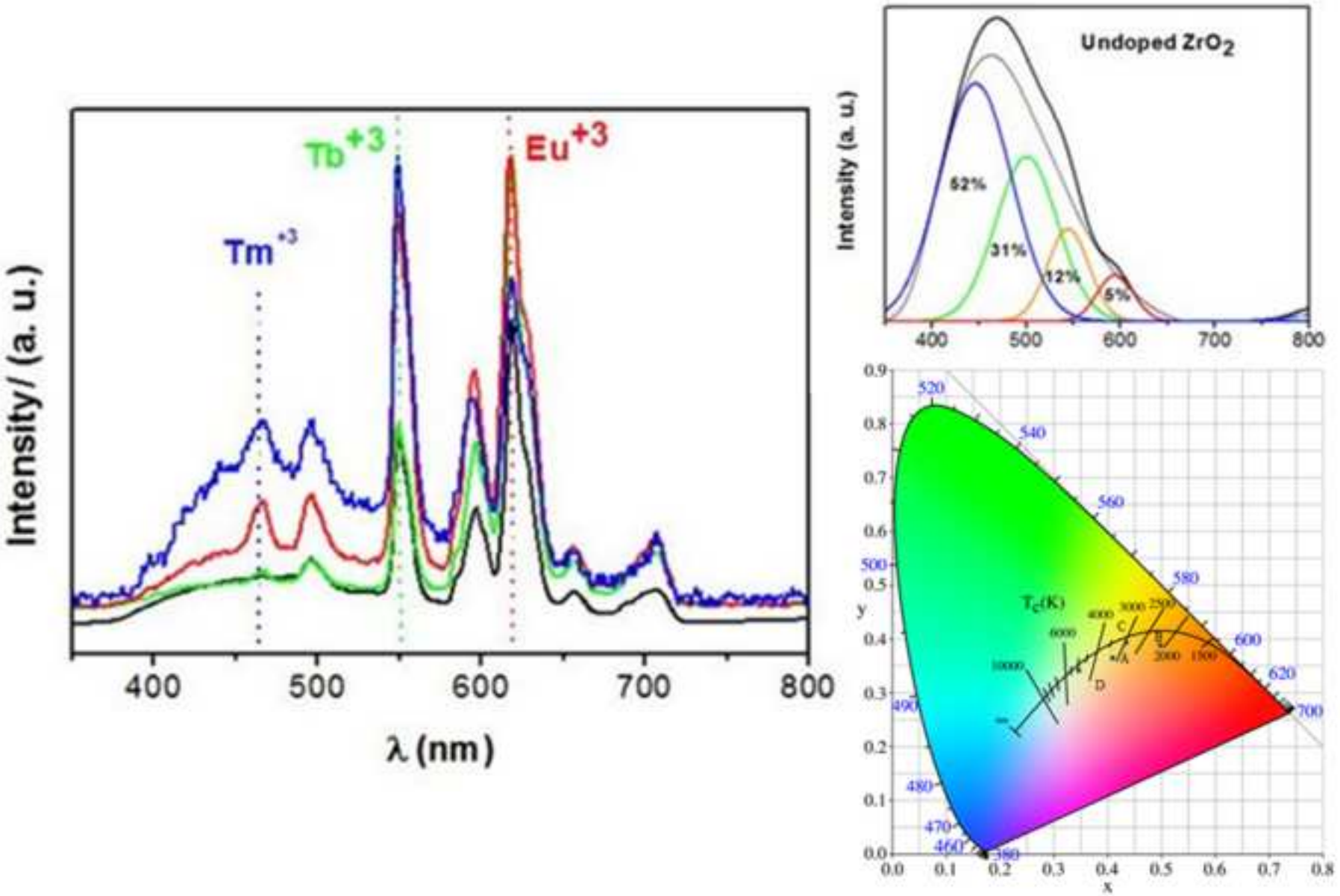

Highlights

The ZrO_2:RE materials presented here are promising photoluminescent materials.

These particles were successfully obtained by the complex polymerization method.

Calculations based on density functional theory were compared to experimental data.

The CIE coordinates calculated are disposed in the blank region in the CIE diagram.

Table 1

Table 1 - Value of structural parameters of ZrO_2:xRE (0 - 8 mol%) nanophosphors

Parameters	ZrO_2	ZrO_2:1%RE	ZrO_2:2%RE	ZrO_2:4%RE	ZrO_2:8%RE
Crystal Sistem	Tetragonal	Tetragonal	Tetragonal	Tetragonal	Cubic
Space group	P42/nmc	P42/nmc	P42/nmc	P42/nmc	Fm-3m
2θ	30.0266	29.9272	29.8368	30.1498	29.8368
FWHM (rad)	0.3149	0.7872	0.3149	0.9446	0.3936
Lattice parameters (Å)					
a	3.59756	3.61069	3.60521	3.62814	5.15833
c	5.19462	5.20999	5.19164	5.14336	-
Unit cell volume/formula unit ($Å^3$)	67.2312	67.9231	67.4786	67.7040	137.2545
Crystallite size (nm)	14.06	14.49	14.79	14.62	12.78

Table 2

Table 2 – Active raman modes, space group and c/a lattice parameter ratio for the zirconia polymorphs

Crystal system	Space group	Active raman modes	c/a
Tetragonal	D_{4h}	$A_{1g} + 2B_{1g} + 3E_g$	> 1
Cubic	O_h	T_{2g}	= 1

Table 3

Table 3: Distances in Å for the coordination polyhedra for doped ZrO_2 with Eu^{+3} for the cubic and tetragonal phases.

cubic					tetragonal				
Symbol	Ligands	Faces	Dmin	Dmax	Symbol	Ligands	Faces	Dmin	Dmax
Eu1	8	12	2.281	2.471	Eu1	7	8	2.286	2.368
Eu2	8	10	2.308	2.459	Eu2	8	11	2.331	2.512
Zr1	8	12	2.071	2.611	Zr1	7	10	2.044	2.394
Zr2	8	12	2.061	2.568	Zr2	8	12	2.081	2.48
Zr3	7	9	2.079	2.184	Zr3	8	12	2.063	2.617
Zr4	8	10	2.091	2.265	Zr4	8	12	2.055	2.501
Zr5	8	12	2.066	2.487	Zr5	8	12	2.108	2.376
Zr6	7	10	2.054	2.218	Zr6	8	12	2.141	2.269
Zr7	8	12	2.141	2.347	Zr7	8	12	2.118	2.391
Zr8	8	12	2.11	2.326	Zr8	7	10	2.071	2.297
Zr9	7	9	2.006	2.303	Zr9	8	12	2.127	2.44
Zr10	7	10	2.041	2.267	Zr10	8	12	2.098	2.685
Zr11	8	12	2.131	2.268	Zr11	8	12	2.118	2.391
Zr12	7	10	2.089	2.206	Zr12	7	10	2.071	2.297
Zr13	7	9	2.058	2.219	Zr13	8	12	2.127	2.44
Zr14	7	10	2.069	2.261	Zr14	8	12	2.098	2.685

Table 4

Table 4 - Chromaticity coordinates and correlated temperature color for ZrO_2:xRE (x: 1, 2, 4 and 8 mol%)

Sample	x	y	CCT (K)	Color
ZrO_2: 1% Eu	0.41	0.36	3.174	yellow
ZrO_2: 2% Eu	0.50	0.37	1.988	orange
ZrO_2: 4% Eu	0.43	0.38	2.917	yellow
ZrO_2: 8% Eu	0.34	0.34	5.181	white

Figure 1

Click here to download high resolution image

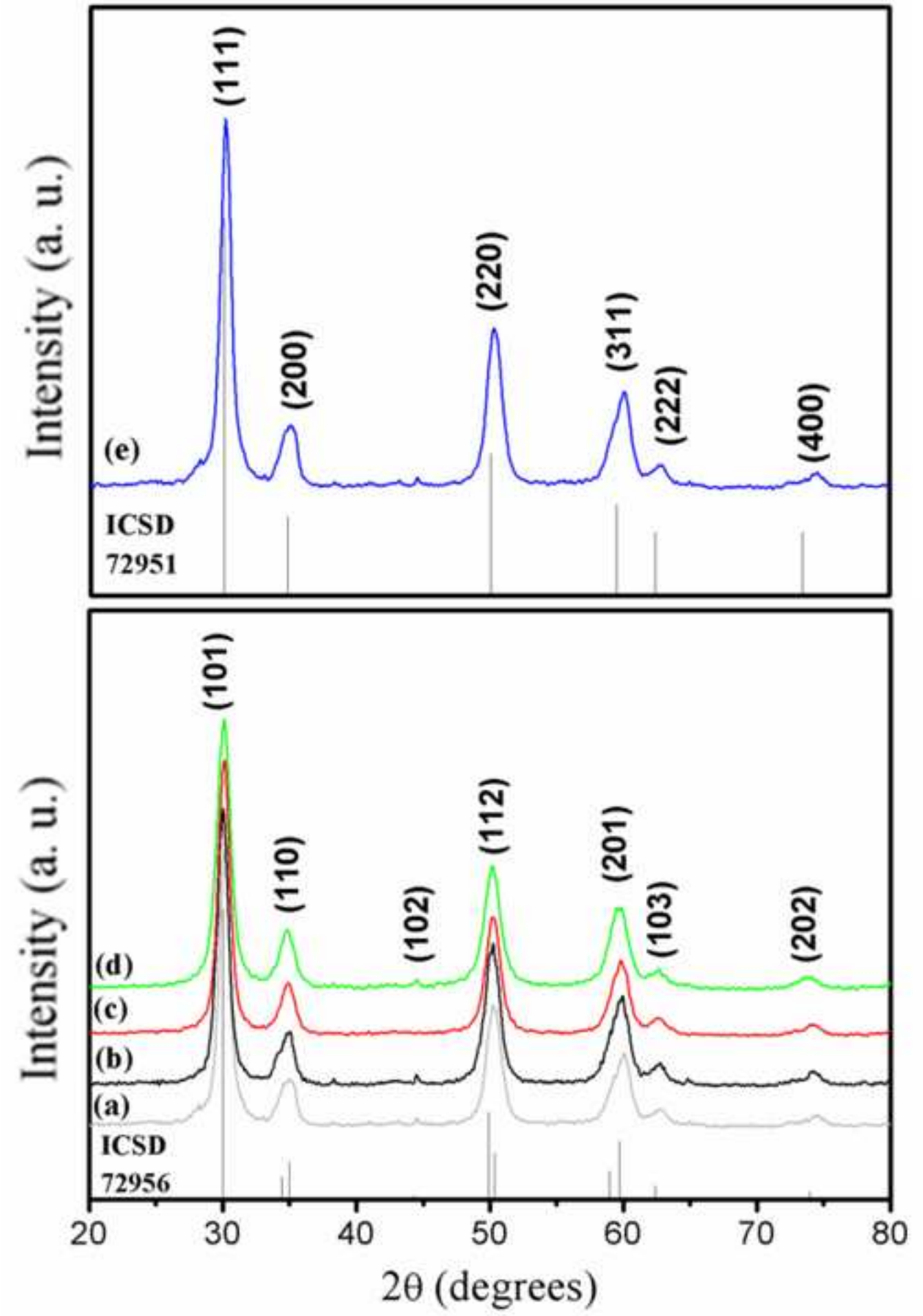

Figure 2

Click here to download high resolution image

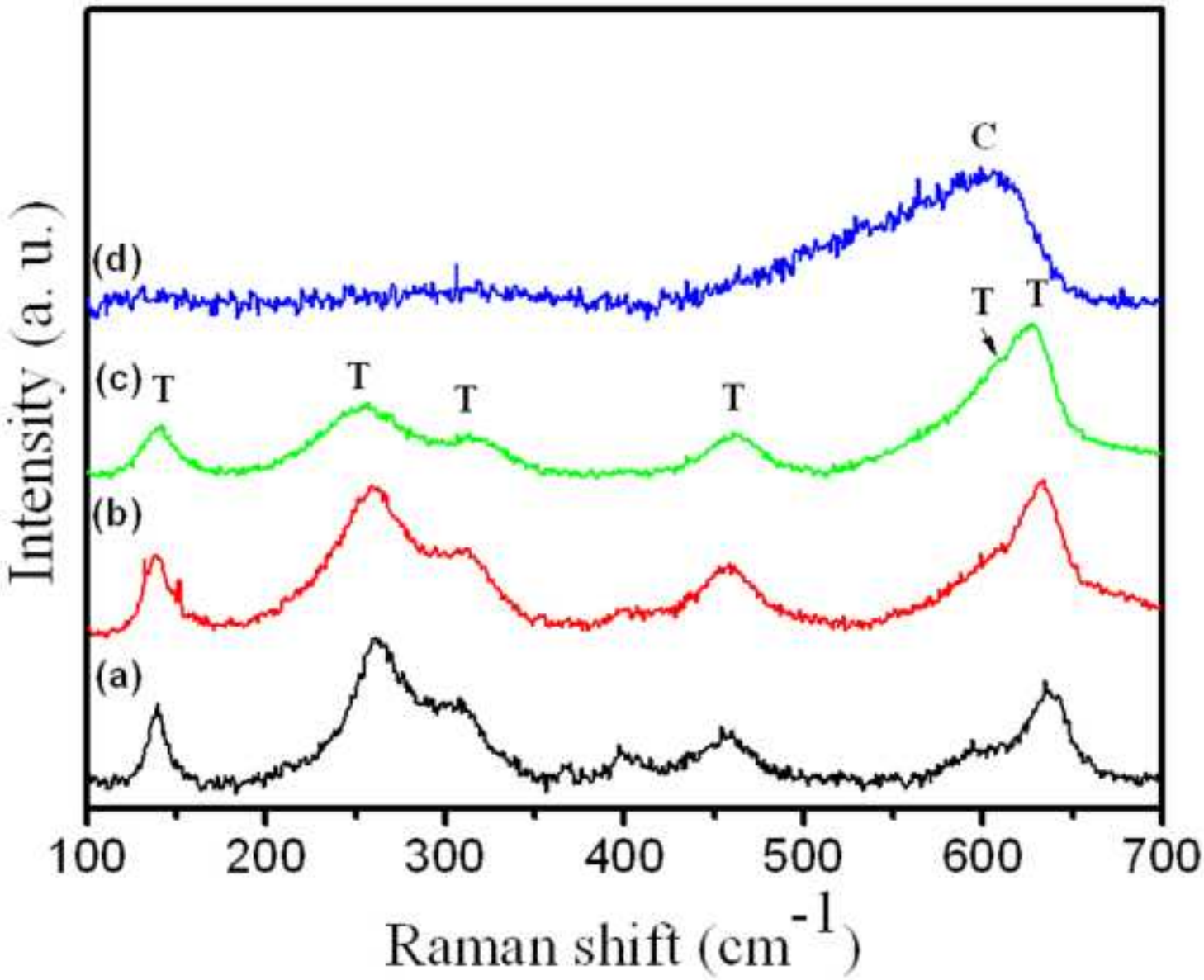

Figure 3

Click here to download high resolution image

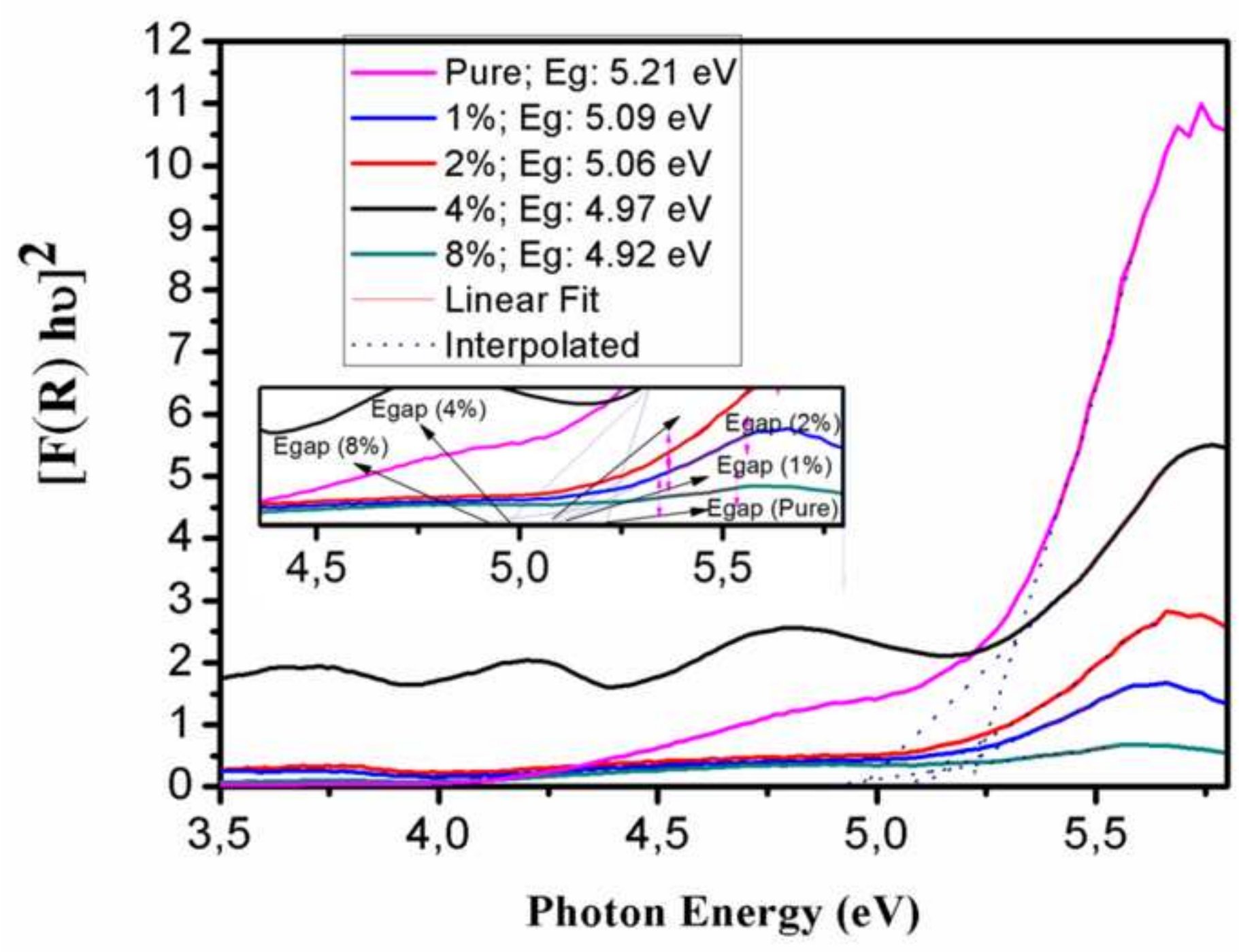

Figure 4

Click here to download high resolution image

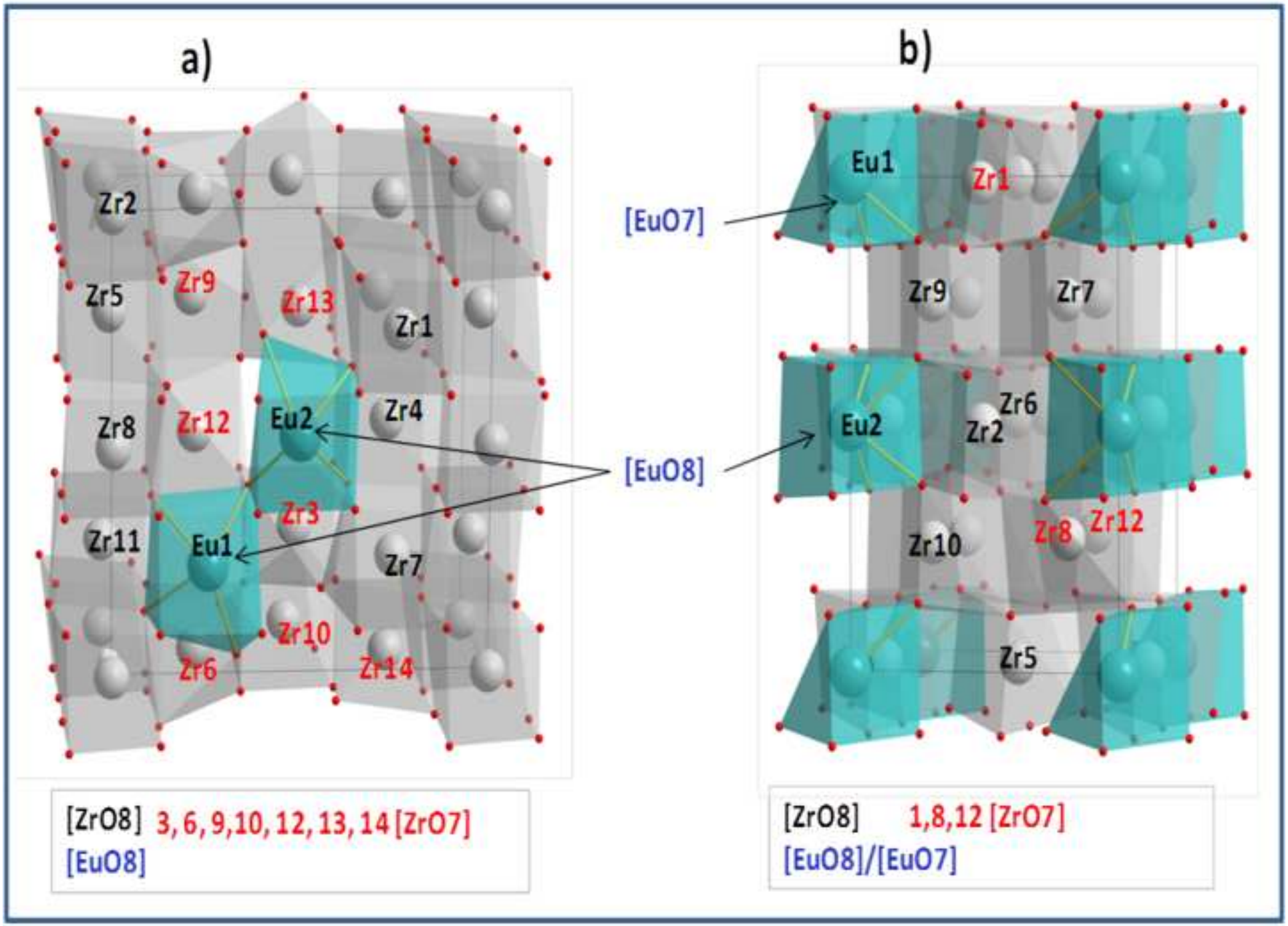

Figure 5

Click here to download high resolution image

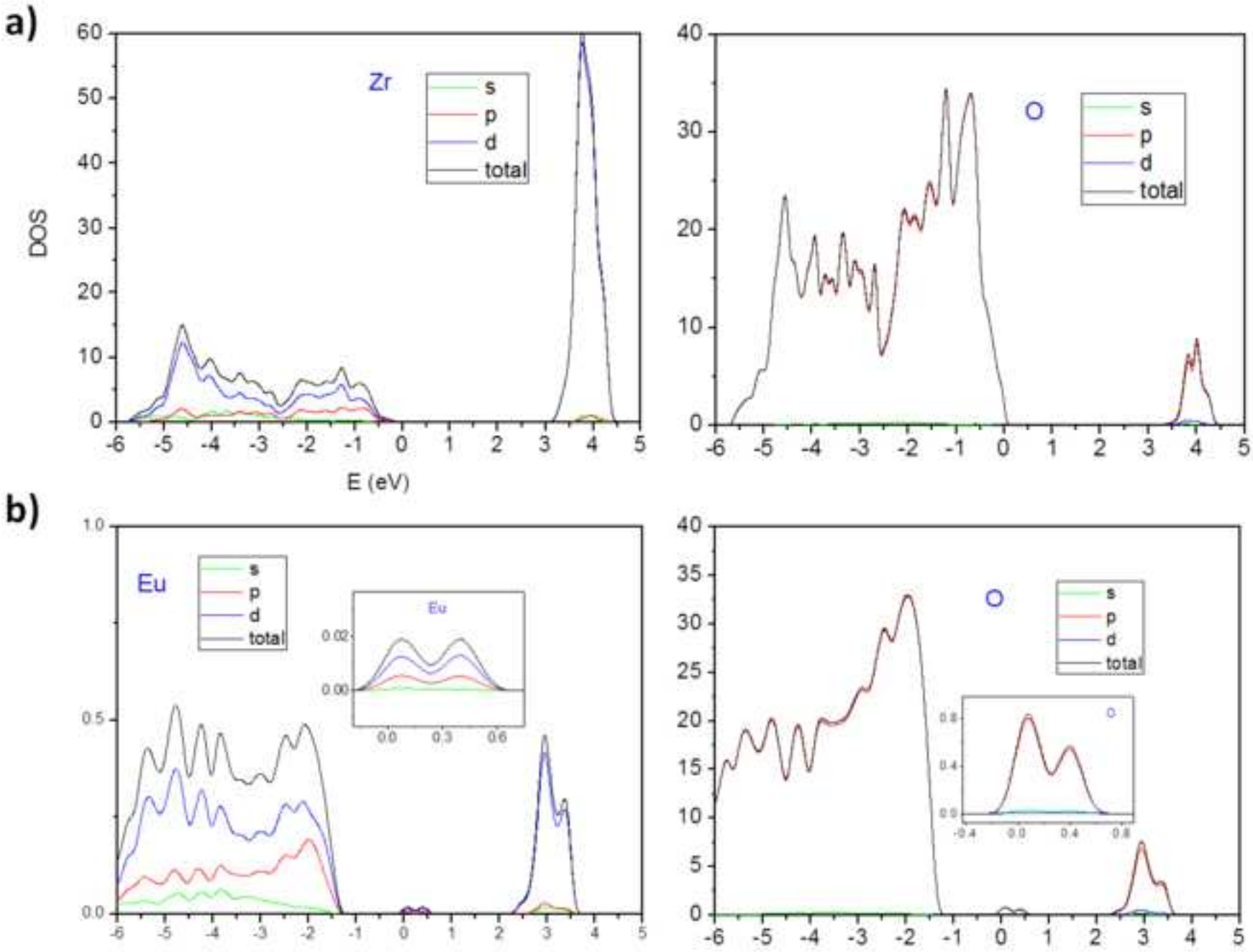

Figure 6

Click here to download high resolution image

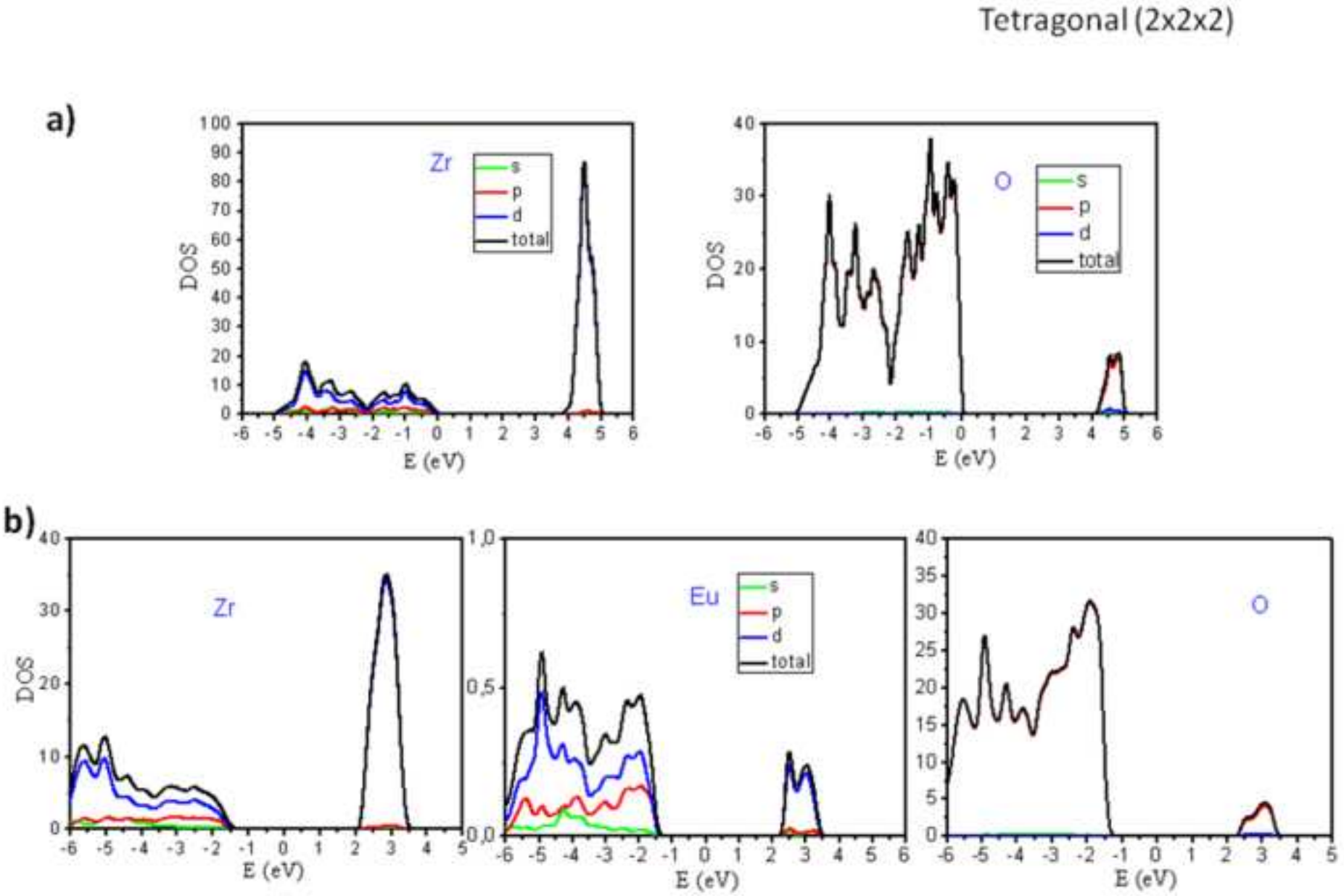

Figure 7

Click here to download high resolution image

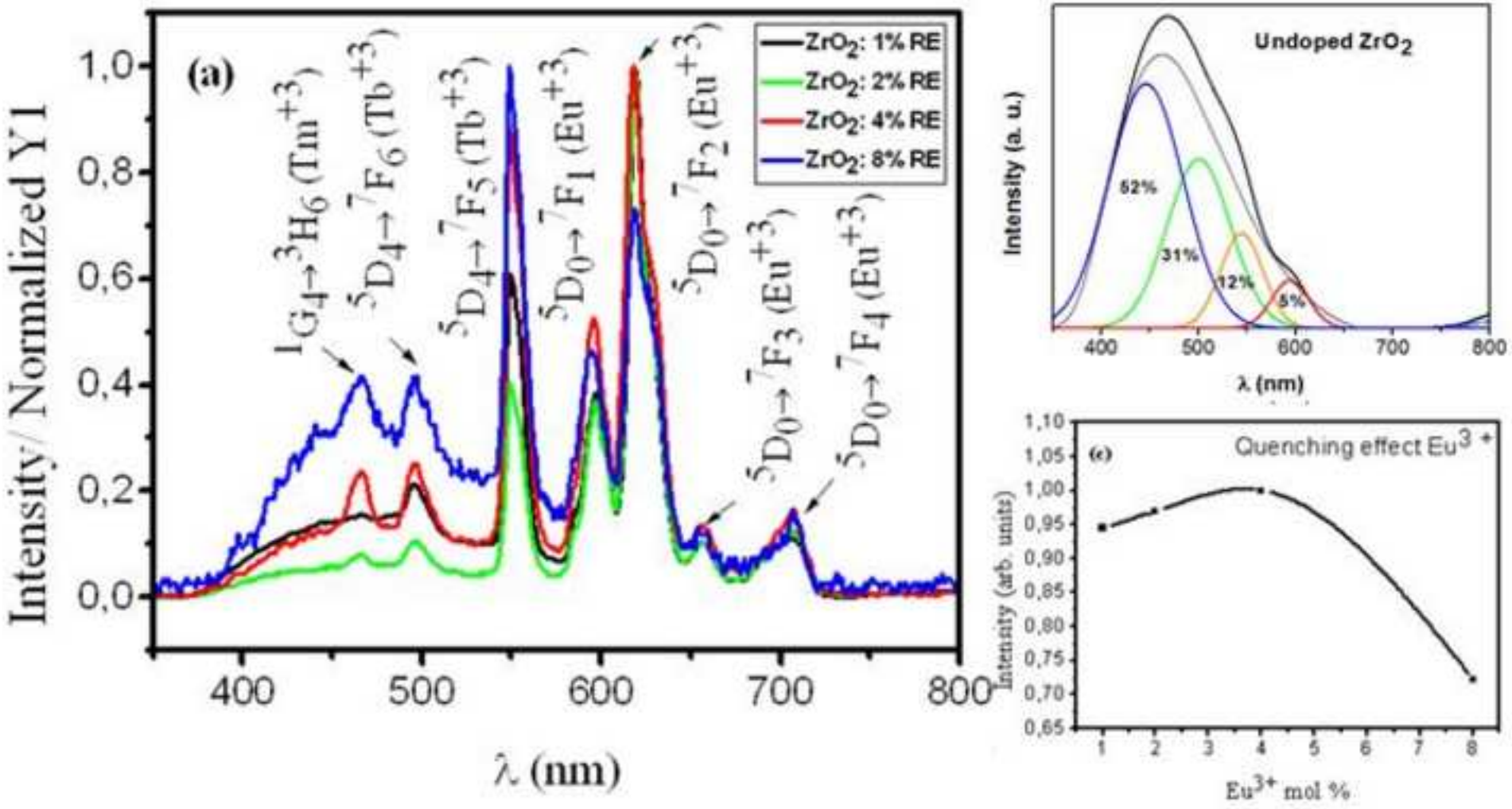

Figure 8

Click here to download high resolution image

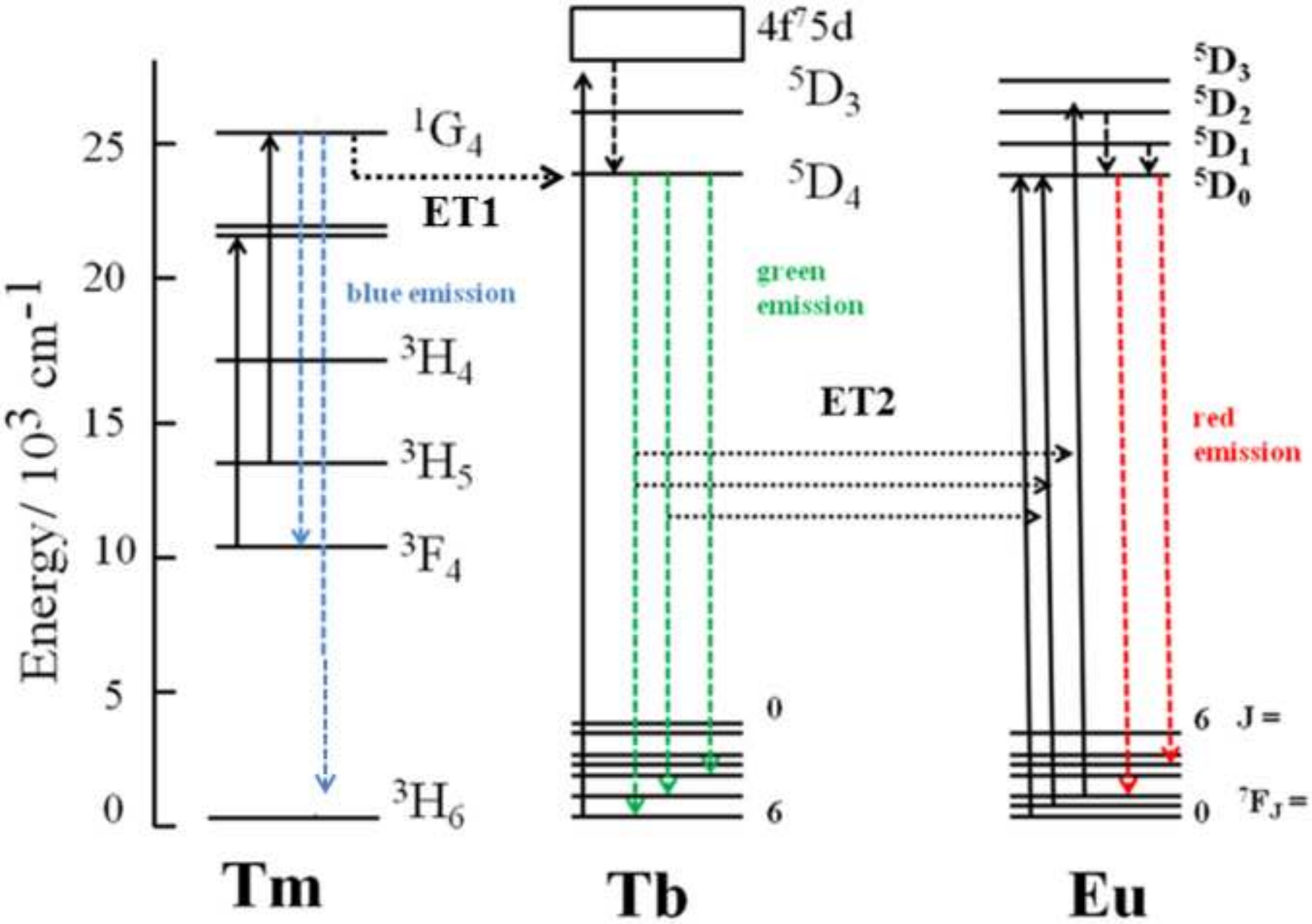

Figure 9

Click here to download high resolution image

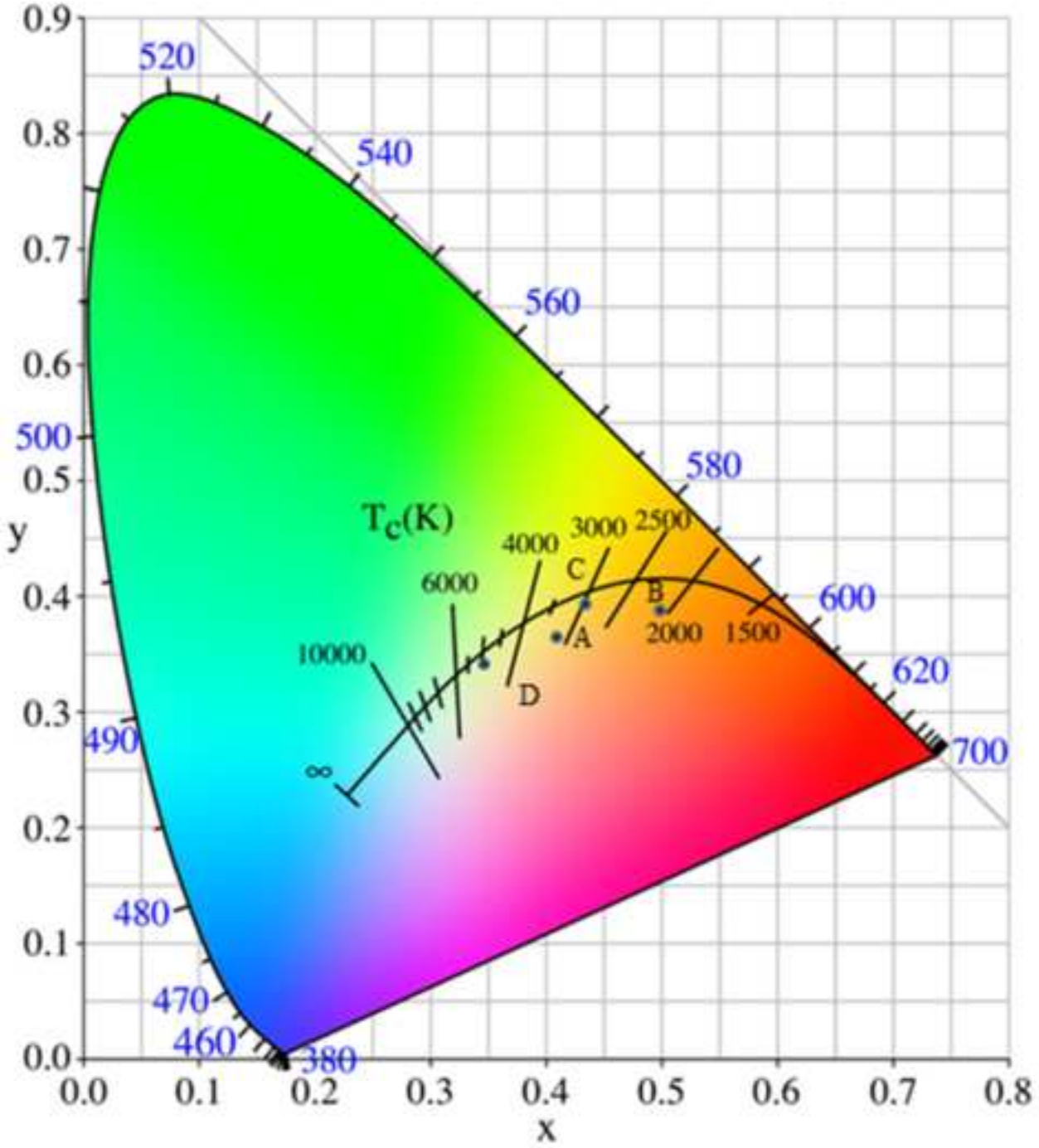

Supplementary Material for on-line publication only

Click here to download Supplementary Material for on-line publication only: Supplementary Information.docx